Article

Deep, ancient melting recorded by ultralow oxygen fugacity in peridotites

https://doi.org/10.1038/s41586-024-07603-w

Received: 25 July 2022

Accepted: 23 May 2024

Check for updates

Suzanne K. Birner[1]✉, Elizabeth Cottrell[2], Fred A. Davis[3] & Jessica M. Warren[4]

The oxygen fugacity (f_{O2}) of convecting upper mantle recorded by ridge peridotites varies by more than four orders of magnitude[1–3]. Although much attention has been given to mechanisms that drive variations in mantle f_{O2} between tectonic settings[1,3,4] and to comparisons of f_{O2} between modern and ancient-mantle-derived rocks[5–10], comparatively little has been done to understand the origins of the high variability in f_{O2} recorded by rocks from modern mid-ocean ridge settings. Here we report the petrography and geochemistry of peridotites from the Gakkel Ridge and East Pacific Rise (EPR), including 16 new high-precision determinations of f_{O2}. Refractory peridotites from the Gakkel Ridge record f_{O2} more than four orders of magnitude below the mantle average. With thermodynamic and mineral partitioning modelling, we show that excursions to ultralow f_{O2} can be produced by large degrees of melting at high potential temperature (T_p), beginning in the garnet field and continuing into the spinel field—conditions met during the generation of ancient komatiites but not modern basalts. This does not mean that ambient convecting upper mantle had a lower ferric to ferrous ratio in Archaean times than today nor that modern melting in the garnet field at hotspots produce reduced magmas. Rather, it implies that rafts of ancient, refractory, ultrareduced mantle continue to circulate in the modern mantle while contributing little to modern ridge volcanism.

f_{O2} reflects complex activity–composition relationships among mantle minerals and melts that govern the oxidation states of multivalent elements—relationships that bear on the depth of mantle melting[11], the speciation of volatiles[12], ancient surface environments[13,14] and mantle evolution[4]. The f_{O2} recorded by mid-ocean ridge basalt (MORB) glasses is near the quartz–fayalite–magnetite (QFM) buffer and varies over a narrow range of less than a log unit[15–17]. Ridge-derived peridotites also record an average f_{O2} near QFM, but these rocks record f_{O2} values that vary by orders of magnitude, suggesting a heterogeneous sub-ridge mantle both globally and on the scale of individual dredges[1,2]. This redox heterogeneity within mid-ocean ridge peridotites may reflect modern ridge processes or pre-existing heterogeneities developed before emplacement beneath the ridge axis. Both possibilities have important implications for the generation of oceanic crust.

Major and trace-element chemistry of mid-ocean ridge peridotites demonstrates that compositional variability can be generated at the ridge owing to processes such as melting and melt–rock interaction[18,19], subsolidus re-equilibration during cooling[2,20] and low-temperature alteration[21]. However, there is no evidence that these processes generate notable variation in f_{O2} (refs. 22–25), indicating that variations instead reflect pre-existing heterogeneity. Isotopic evidence suggests that the modern mantle is heterogeneous, juxtaposing domains of varying lithology[26,27], provenance[28–30] and fertility[31,32]. Here we investigate ridge peridotites from several locations, focusing on refractory harzburgites—peridotites that record large degrees of melt extraction. These samples may retain a record of ancient melting events[31–33] while contributing less to modern ridge melts than fertile peridotites[19,34,35].

Low f_{O2} in some refractory harzburgites

We use the Mössbauer-calibrated microprobe technique[36,37] to provide high-precision f_{O2} measurements of peridotites from the Gakkel Ridge[32] ($n = 10$) and from Hess Deep[38] ($n = 6$), near the EPR. We also interpret peridotites from the Southwest Indian Ridge (SWIR; $n = 26$) with previously published f_{O2} and major/trace-element data[2,25]. Samples comprise lherzolites and harzburgites and we limit our discussion to samples with little evidence of melt–rock interaction[25]. When discussing lherzolites, we use the term 'residual' to refer to non-melt-influenced samples whose chemical variations are expected to be driven primarily by the extraction of melt[25]. We focus on harzburgites that are particularly refractory (that is, melt-depleted), having less than about 1% clinopyroxene.

Residual lherzolites from the ultraslow-spreading SWIR and Gakkel Ridge record f_{O2} values consistent with the global ridge peridotite and MORB datasets. By contrast, refractory harzburgites from the SWIR and Gakkel Ridge record f_{O2} values orders of magnitude more reduced (Fig. 1 and Supplementary Table 1). This is particularly true at Gakkel Ridge, at which spinel $Fe^{3+}/\Sigma Fe$ ratios ($Fe^{3+}/(Fe^2 + Fe^{3+})$) can be indistinguishable from 0 ($Fe^{3+}/\Sigma Fe \leq 0.03$, equating to $f_{O2} \leq$ QFM-2; Extended Data Fig. 1). At both the SWIR and Gakkel Ridge, the refractory harzburgites record much lower f_{O2} than the residual lherzolites ($P < 0.01$) and much

[1]Division of Natural Sciences, Nursing, and Mathematics, Berea College, Berea, KY, USA. [2]National Museum of Natural History, Smithsonian Institution, Washington, DC, USA. [3]Department of Earth and Environmental Sciences, University of Minnesota Duluth, Duluth, MN, USA. [4]Department of Earth Sciences, University of Delaware, Newark, DE, USA. ✉e-mail: birners@berea.edu

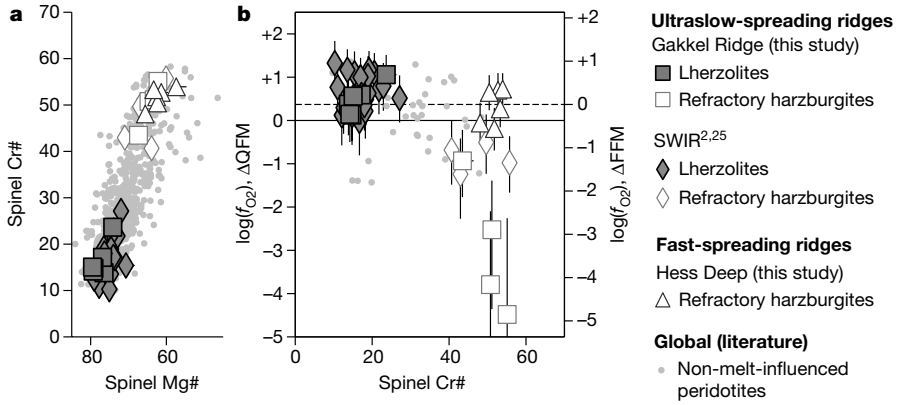

Q12

Fig. 1 | Natural peridotite data. Geochemistry and f_{O2} results for non-melt-influenced[25] mid-ocean ridge peridotites. **a**, Spinel Cr# versus spinel Mg#. Residual lherzolites from the SWIR and Gakkel Ridge record low spinel Cr# (<30), whereas refractory harzburgites from the SWIR, Gakkel Ridge and Hess Deep record high spinel Cr# (>40). Error bars represent 1 s.d. for all spinel probe analyses performed for each sample. Global data are from the residual (non-melt-influenced) dataset of ref. 19. **b**, log(f_{O2}), relative to the QFM buffer, versus spinel Cr#. Refractory harzburgites record a much wider range in f_{O2} than residual lherzolites. Although refractory harzburgites from Hess Deep record f_{O2} values that are statistically indistinguishable from the residual lherzolite array, refractory harzburgites at the SWIR and Gakkel Ridge fall to substantially more reduced values. Error bars for spinel Cr# represent 1 s.d. (as in panel **a**), whereas error bars for log(f_{O2}) represent total uncertainty[37]. Global data are from ref. 1 recalculated[2,37] at recorded conditions of approximately 900 °C and 0.6 GPa (see Methods). The right axis shows f_{O2} values relative to the FFM buffer. Although the offset between ΔFFM and ΔQFM values is a function of the temperature of each sample, these variations are imperceptible on the scale of this plot ($1\sigma_{offset\_values}$ = 0.02 log units) and the offset can thus be treated as a constant $offset_{\Delta FFM\text{-}\Delta QFM}$ = 0.37 log units.

lower f_{O2} than global residual ridge samples ($P < 0.01$; see Methods for statistical details). As well as their low f_{O2}, the refractory harzburgites at the Gakkel Ridge and SWIR share other key geochemical attributes associated with large degrees of melt extraction, including high spinel Cr#, lack of clinopyroxene and depleted heavy rare earth element (HREE) contents (Extended Data Fig. 1).

Samples from Hess Deep, associated with the fast-spreading EPR, record many of the same geochemical attributes (little to no clinopyroxene, high Cr# and depleted HREEs[39]); however, they do not record low f_{O2} (Fig. 1 and Supplementary Table 1). Instead, the Hess Deep peridotites record f_{O2} near QFM, consistent with residual lherzolites from the SWIR and Gakkel Ridge, and with the f_{O2} of MORBs. Thus, a successful model must explain the occurrence of refractory harzburgites at the Gakkel Ridge/SWIR that are strongly reduced, as well as the occurrence of residual lherzolites at the Gakkel Ridge/SWIR and harzburgites at Hess Deep that record f_{O2} typical of modern MORB mantle.

Refractory mantle from fast-spreading or high T_p

Hess Deep harzburgites have undergone large degrees of melting at the fast-spreading EPR[38,39], with possible further melting within the Cocos–Nazca rift[40]. Owing to its spreading rate, the EPR features a thin conductive cooling lid, which allows melting to continue to shallow conditions, producing a thick basaltic crust[41] and refractory residual peridotites that record removal of high melt fractions (F = 15–20%)[39].

Our observation that high-F harzburgites from Hess Deep record f_{O2} consistent with residual lherzolites measured at the SWIR and Gakkel Ridge suggests that modern melt extraction does not strongly affect f_{O2}, consistent with observations from ref. 25 demonstrating that spinel Cr# (a proxy for F) and f_{O2} do not correlate for low to moderate degrees of melting. This is also consistent with measurements from basalts, which show no trend in f_{O2} with proxies for melt fraction such as Na8 (refs. 17,42) and with Fe^{3+} partitioning experiments, which suggest little change in F over a range of f_{O2} (refs. 23,24).

As with the Hess Deep harzburgites, the high-Cr# spinels, lack of clinopyroxene and depleted HREE contents of the SWIR/Gakkel Ridge refractory harzburgites suggest that these samples have undergone large degrees of melt extraction. However, based on geochemical and geophysical observations, high extents of melting did not occur beneath the modern ridge axis and instead reflect ancient melting events. Geophysical observations indicate a thin basaltic crust at the Gakkel Ridge[43], consistent with a thick conductive cooling lid and general lack of magmatism resulting from the ultraslow spreading rate of the ridge[44,45]. Although this observation is consistent with the low F (<10%) implied by Gakkel Ridge lherzolites, it is inconsistent with the much larger F needed to produce the Gakkel Ridge harzburgites[19,32]. Furthermore, unradiogenic Os and Hf isotopic ratios in a subset of the Gakkel Ridge and SWIR peridotites, and ridges globally, support an association between large degrees of melting and ancient melting events[31,33,46,47]. However, constraining age remains difficult because of the challenges of measuring extremely depleted isotopic ratios and the possibility of later modification of isotopic values by melt–rock interaction[29,33].

Ancient melting events in a hotter mantle would have begun deeper, resulting in larger melt fractions and more refractory residues[48,49]. Thus, ancient melting at high T_p provides an alternative mechanism to modern melting at fast-spreading ridges for producing refractory peridotite residues. In contrast to the Hess Deep peridotites, we interpret the refractory peridotites from the SWIR/Gakkel Ridge as having formed during ancient, high-T_p melting events.

Low-f_{O2} residues from high-T_p melting

To assess the evolution of f_{O2} during mantle melting, we used two melting models: pMELTS and an empirical model. For each of these, we calculated f_{O2} at each step from the mineral compositions of the model using the spinel oxybarometer formulation in ref. 37. Our goal was to explore the underlying chemical and thermodynamic controls on f_{O2} as a function of T_p, degree of melting and stable phase assemblage. Each model is described briefly below and extensively in Methods.

The pMELTS thermodynamic framework[50] predicts stable mineral ± melt assemblages using a free-energy minimization routine. The benefits of pMELTS include its internally consistent thermodynamic library for solid-phase relations and the flexibility it allows for computational modelling of mantle processes[50,51]. However, pMELTS has important shortcomings when modelling f_{O2}, including the exclusion of Fe^{3+} from garnet and the overstabilization of spinel[51], a lack of fidelity between thermodynamic predictions and experiments at pressures

>3 GPa (ref. 50) and a lack of equilibrium between melt f_{O_2} and solid f_{O_2} (refs. 24,52).

For comparison with pMELTS, we developed an empirical model based on natural and experimental data. This model calculates the evolution of melts and residues during adiabatic decompression using mass balance and empirical partitioning constraints, incorporating Fe^{3+} into spinel, garnet, both pyroxenes and the melt phase. We determined partitioning relationships to govern the distribution of each element from a combination of xenolith data and experimental data (Methods). A key innovation of our empirical model is that we include experimental constraints on Fe^{3+} partitioning between peridotitic spinel and melt[24,52].

In our samples, f_{O_2} is constrained by equilibrium between olivine, orthopyroxene and spinel. We thus normalize our model results to the fayalite–ferrosilite–magnetite (FFM) buffer, representing the f_{O_2} of an assemblage of pure fayalite (Fe_2SiO_4), ferrosilite ($Fe_2Si_2O_6$) and magnetite (Fe_3O_4). Divergences of natural or modelled spinel peridotite compositions from the FFM buffer thus reflect only changes in the activities of these endmembers within olivine, orthopyroxene and spinel (Methods and Extended Data Fig. 2). Versions of Figs. 2 and 3 relative to QFM are included for comparison in Extended Data Fig. 3.

Because Earth's mantle has cooled over time, ancient melting events would have initiated deeper, leading to greater degrees of melt extraction[48,49]. To test the implications for harzburgite chemistry, we modelled adiabatic decompression paths for peridotite at T_p = 1,350–1,550 °C (see Methods). In both models, mantle assemblages at higher T_p melt deeper, produce higher F for a given pressure and record much lower f_{O_2} at a given degree of melt extraction in the spinel field (Fig. 2a,b). Unlike the model of ref. 53, which also predicts lower f_{O_2} at higher temperature, our model does not predict notable evolution of f_{O_2} during spinel-field melting (Fig. 2a,b).

In pMELTS and our empirical model, we see the same subsolidus features observed by refs. 51,54: (1) f_{O_2} decreases as the solid assemblage decompresses from the garnet field to the spinel field and (2) f_{O_2} decreases slightly as potential temperature increases. We show here that further, irreversible reduction occurs during high potential temperature melting in the garnet field.

Passive decrease in f_{O_2} during garnet-out

Across our models, we observe a decrease in f_{O_2} as pressure decreases towards garnet-out, followed by little to no change in f_{O_2} as pressure decreases through the spinel field (Fig. 2). This decrease in f_{O_2} during the garnet-to-spinel transition has been previously described in ref. 51 as a passive dilution effect owing to consumption of Al-rich garnet to produce pyroxene and spinel, which lowers the concentration of ('dilutes') Fe^{3+} in these last phases. Although pMELTS does not incorporate Fe^{3+} into garnet, modelling in ref. 51 in PerpleX, which does incorporate Fe^{3+} into garnet, shows a similar decrease in f_{O_2} compared with pMELTS in the approximately 1 GPa pressure interval in which garnet transitions to spinel. Our empirical model, which includes Fe^{3+} in garnet, suggests an even larger decrease in f_{O_2} in this pressure interval than that predicted by pMELTS (see Methods). Across models, f_{O_2} decreases because Fe^{3+} concentrations are diluted in spinel and orthopyroxene as their modes increase at the expense of garnet (Extended Data Figs. 4 and 5). This dilution takes place as long as the initial Fe^{3+}/Al^{3+} ratio of garnet is lower than that of orthopyroxene and spinel, such that spinels and pyroxenes after garnet-out contain proportionally less Fe^{3+} than at the start of the garnet-to-spinel transition. All modelled garnets have low Fe^{3+}/Al ratios (in pMELTS, the ratio is zero), which explains why this result transcends the limitation imposed by the exclusion of Fe^{3+} from garnet in pMELTS.

Regardless of the model used (pMELTS, PerpleX or our empirical model) or reference frame (ΔQFM, ΔFFM or absolute f_{O_2}), a robust feature is that the f_{O_2} of garnet peridotite decreases as it ascends and enters the spinel stability field (Fig. 2). This decrease in f_{O_2} during decompression seems to be in contrast to the expected mantle behaviour based on the continental xenolith record, in which f_{O_2} increases relative to the QFM buffer as pressure decreases as a result of the volume change of the olivine–pyroxene–garnet redox reaction, which favours Fe^{3+} in garnet at depth[4,49,55]. However, the models and natural observations are not

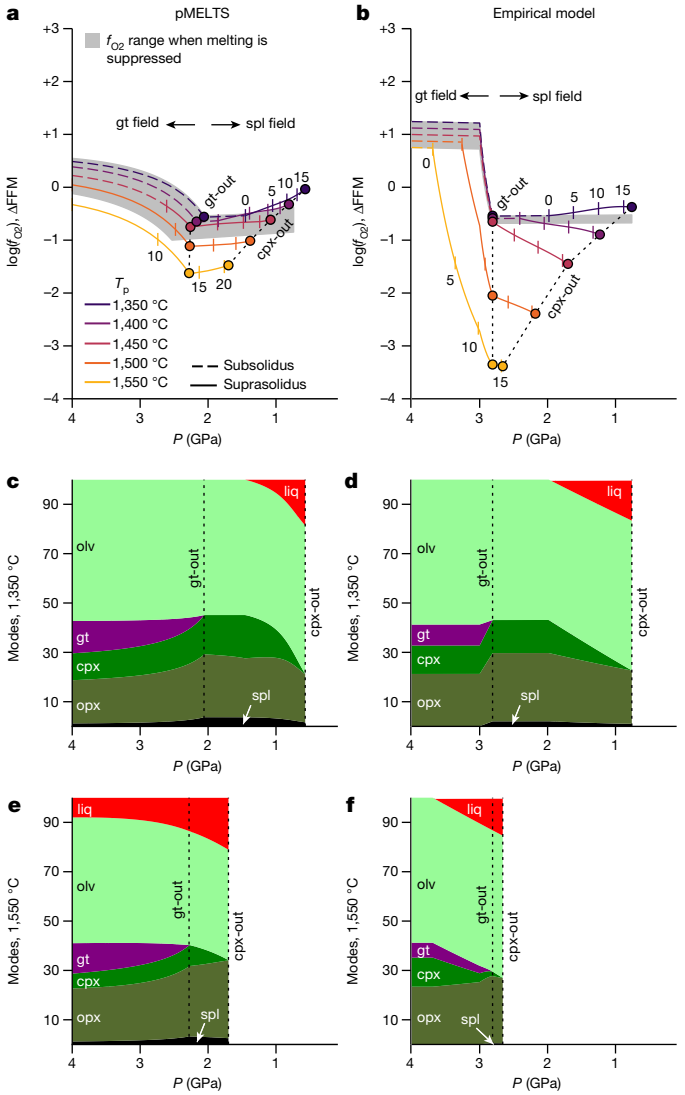

Fig. 2 | Modelling results. Results of pMELTS and our empirical model, demonstrating the effect of potential temperature and composition on f_{O_2} along adiabatic decompression pathways relative to the FFM buffer (see Extended Data Fig. 3 for f_{O_2} relative to QFM). **a**,**b**, Oxygen fugacity versus pressure at a range of T_p conditions for the pMELTS model (**a**) and our empirical model (**b**). Dashed lines represent subsolidus conditions and solid lines represent conditions in which melt is present. Grey-shaded regions show the range of model results when melting is suppressed, demonstrating the effect of potential temperature alone. Tick marks demarcate 5-degree increments in melt fraction (F). Paths at potential temperatures approximately ≤1,450 °C, at which melting occurs only in the spinel field, record a relatively narrow range of f_{O_2}. Paths at higher potential temperature fall to substantially more reduced f_{O_2} owing to the extra effect of garnet-field melting. **c**,**d**, Modal abundances for 1,350 °C melting paths. As pressure decreases, garnet reacts to form pyroxene and spinel. Melting begins in the spinel stability field, reaching clinopyroxene-out at pressures shallower than 1 GPa. **e**,**f**, Modal abundances for 1,550 °C melting paths. Melting begins in the garnet field, resulting in higher melt fraction at a given pressure when compared with the 1,350 °C melting paths. At cpx-out, melting paths at 1,550 °C contain higher modes of ferric-bearing minerals (orthopyroxene + spinel) when compared with the 1,350 °C melting paths, resulting in lower Fe_2O_3 concentrations in these phases, as the bulk Fe_2O_3 must be shared across the total mass of ferric-bearing minerals.

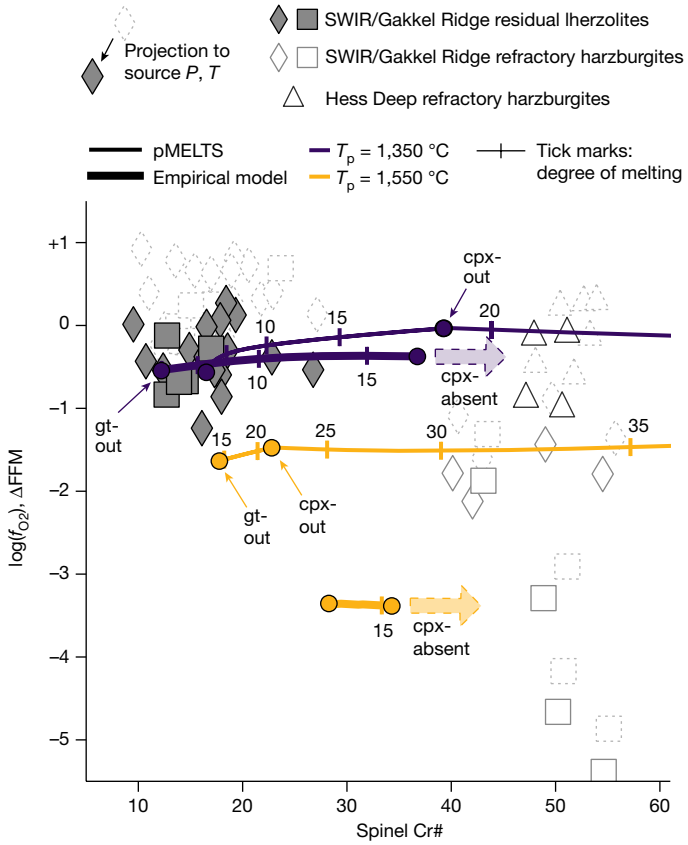

Fig. 3 | Comparison of natural data and models. Oxygen fugacity versus spinel Cr# in the spinel stability field. Natural data symbols: dotted, f_{O2} calculated according to ref. 37, as in Fig. 1; solid outlines, f_{O2} projected to the pressure and temperature conditions of basalt extraction for each location relative to the solid buffer using the iso-compositional + exchange reaction projections of ref. 2. Our projection lowers peridotite f_{O2} by about 0.5–1.0 log units (Supplementary Table 1). SWIR and Gakkel Ridge peridotites are projected to 1.25 GPa and 1,320 °C (the conditions of basalt extraction determined from SWIR basalts[2]). Hess Deep peridotites are projected to shallower conditions of 0.6 GPa and 1,307.51 °C. These conditions were chosen from our T_p = 1,350 °C pMELTS model output (initial composition = DMM) to match the estimated degree of melting of the Hess Deep peridotites (F = 17.5% (ref. 39)). In no case does the choice of projection conditions lead to notable differences between the sample groups. Model: we plot spinel-field results using the pMELTS model and our empirical model. Along a 1,350 °C adiabat, spinel Cr# increases with little evolution in f_{O2}. The empirical model ends at cpx-out, although we indicate that the expected trajectory (dashed arrow) is consistent with pMELTS output at higher degrees of melt extraction. At 1,550 °C, both models show greatly reduced f_{O2} by the time the residue enters the spinel field at garnet-out conditions. Once in the spinel field, little further evolution of f_{O2} occurs, although spinel Cr# continues to increase as melting proceeds.

in conflict; instead, thermodynamic models predict a local maximum in f_{O2} at pressures near the garnet-to-spinel transition[51,54] (Fig. 4a and Extended Data Figs. 2 and 3).

Garnet-field melting generates reduced residues

We show here that ultrareduced residues can be generated by melting at high potential temperature that initiates in the garnet field and continues into the spinel field. In the absence of melting, high T_p alone has a small effect[49]. The grey field in Fig. 2 demonstrates the narrow range of f_{O2} values across modelled T_p when melting is suppressed (that is, the peridotite assemblage is forced to remain subsolidus). Although T_p affects f_{O2} through redistribution of temperature-sensitive elements, this is not the primary factor driving ultrareduced residues. Only when melting is allowed does hotter mantle see substantially greater reduction than cooler mantle (Fig. 2a,b).

To isolate the effects of temperature, melting and garnet, we performed further modelling with melting and/or garnet stability suppressed. Both pMELTS and our empirical model generate more reduced residues at similar extents of melt extraction (for example, clinopyroxene-out) when melting occurs at higher T_p compared with lower T_p, along with further decreases in f_{O2} when melting occurs in the presence of garnet (Extended Data Fig. 6).

Two mechanisms lead to reduction of residual peridotites during high-temperature, garnet-field melting: (1) the bulk partition coefficient for Fe^{3+} is lower during hot, garnet-field melting, leading to more efficient extraction of Fe_2O_3 from the residue and (2) melt extraction in the garnet field leads to further increase in the modal proportions of residual orthopyroxene and spinel (Extended Data Fig. 7), beyond the increase caused by the subsolidus garnet-out reactions described above. The consequence of each mechanism is to lower Fe_2O_3 concentrations in pyroxenes and spinel, which results in a residue that records lower f_{O2}. Although the relative importance of temperature, melt extraction and residual garnet differ between the models (Extended Data Figs. 6 and 7), both pMELTS and our empirical model demonstrate that high-temperature melt extraction in the presence of garnet generates reduced peridotite residues.

Because the ultrareduced f_{O2} signature results from a change in bulk composition and modes driven by melting, a reduced residue generated at high potential temperature in the past will retain its low-f_{O2} signature when brought up along a cooler, modern adiabat. We demonstrate this by re-equilibrating refractory, reduced residues generated at 1,550 °C along a modern 1,350 °C adiabat (Extended Data Fig. 8). These refractory rafts retain their low-f_{O2} signatures and do not melt until depths shallower than about 1 GPa, indicating that reduced domains endure in the modern mantle but do not strongly contribute to aggregated melts at modern ridges.

Comparing the models to ridge peridotite data demonstrates that melt extraction under modern potential temperatures can generate both fertile and refractory residues at similar f_{O2} and a broad range of spinel Cr# (Fig. 3). Residual lherzolites at ultraslow-spreading ridges (for example, the SWIR/Gakkel Ridge) record f_{O2} consistent with low-F melting of peridotite under modern T_p (about 1,350 °C). Harzburgites at fast-spreading ridges (for example, Hess Deep) are well described by continued modern melting to shallower conditions, producing higher Cr# spinels at equivalent f_{O2}. The spinel-field magmas produced by this fertile, lherzolitic mantle serve as the primary source of MORB. By contrast, the high-Cr#, low-f_{O2} refractory harzburgites from ultraslow-spreading ridges cannot be generated by melting along a modern ridge adiabat. Instead, reduced, refractory residues are generated by high degrees of deep, garnet-field melting along an older, hotter adiabat. These refractory rafts retain their low f_{O2} because of their low bulk Fe_2O_3 but do not contribute substantially to modern MORB owing to their refractory nature (Extended Data Fig. 8 and Extended Data Fig. 9 schematic).

Although pMELTS provides a good match for residual, low-Cr# lherzolites, as well as high-Cr# harzburgites from Hess Deep and the SWIR, a subset of Gakkel Ridge high-Cr# harzburgites record f_{O2} values much lower than those predicted by pMELTS. These samples are better matched by our empirical model (Fig. 3). Compared with the experimental data used to build the empirical model, pMELTS overpredicts the concentration of Fe_2O_3 in spinels[24] relative to coexisting melt, which could result in underestimation of Fe^{3+} dilution in these phases during the garnet-to-spinel transition. Other possible explanations include lower initial bulk Fe_2O_3, melting at higher temperatures than modelled here, carbon-rich residues that further reduce $Fe^{3+}/\Sigma Fe$ ratios during production of carbonate melts during redox melting[11] and increased error in estimating f_{O2} at low spinel $Fe^{3+}/\Sigma Fe$

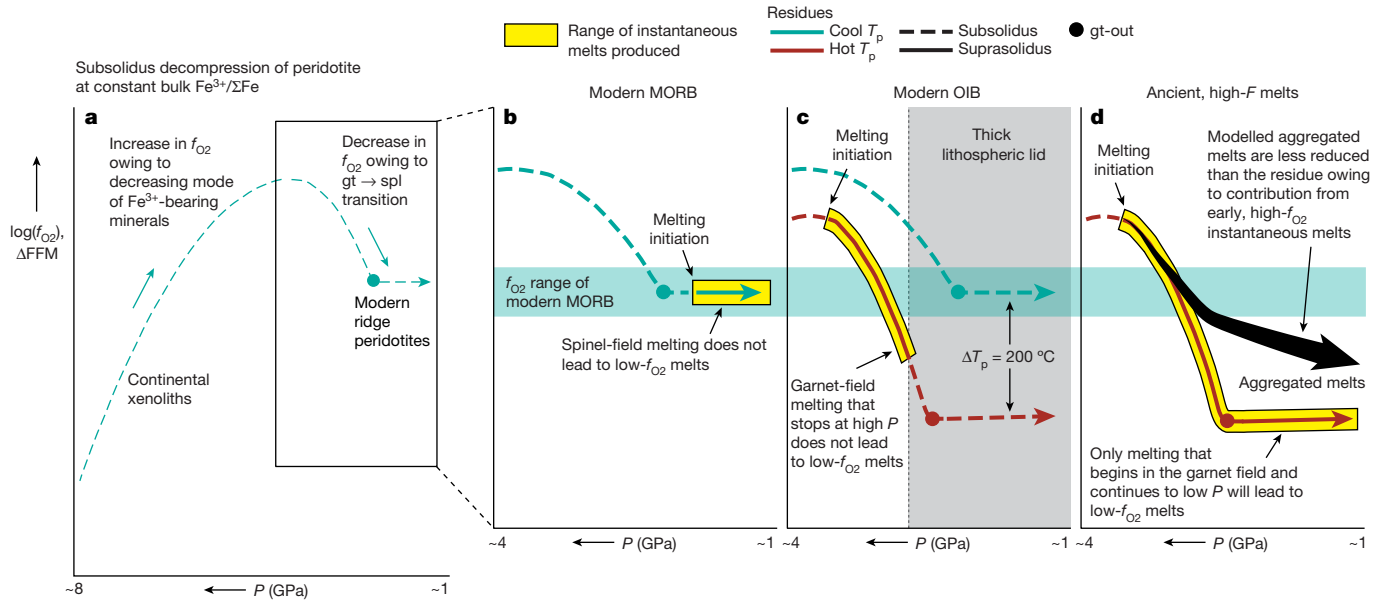

Fig. 4 | Evolution of residues and liquids. Schematic representation of the f_{O2} evolution of residues (dashed/solid lines) and instantaneous melts (yellow highlight). Quantitative liquid f_{O2} models are presented in Extended Data Fig. 10. **a**, Subsolidus upper mantle f_{O2} profile, combining continental xenolith data (about 2–7 GPa) and modelling results (about 1–4 GPa). An f_{O2} maximum is predicted near 4 GPa, with f_{O2} at greater depths controlled by pressure-sensitive changes in the stability of Fe^{3+}-bearing garnet, which increases f_{O2} with decreasing pressure[4,55]. At shallower depths, f_{O2} is controlled by the garnet-to-spinel transition, which decreases f_{O2} with decreasing pressure owing to dilution of Fe^{3+} in spinel and pyroxene[51]. **b**, Beneath modern mid-ocean ridges, mantle decompression along a typical, cool adiabat results in spinel-field melting. Instantaneous melts record f_{O2} consistent with MORB[15–17] and do not evolve strongly in f_{O2} as a function of F. **c**, Beneath modern ocean islands (that is, hotspots), elevated T_p causes deep, garnet-field melting; however, the thick lithospheric lid causes melting to stop at relatively high pressures. Instantaneous melts record a wide range of f_{O2} but without notable melting at shallower depths. Aggregated melts are unlikely to record f_{O2} substantially lower than MORB. **d**, Beneath ancient ridges and hotspots, the f_{O2} range of instantaneous melts is a function of both the pressure of melting onset (determined primarily by T_p) and of melting cessation (determined primarily by lithospheric thickness). The most reduced aggregated melts will be high-F komatiites that began melting at high T_p in the garnet field and continued melting to shallow depth. Aggregated melts will probably not be as reduced as the final residue owing to the influence of deeper, more oxidized melts (Extended Data Fig. 10). Many Archaean basalts may not be reduced if they melted primarily in the spinel field, whereas some komatiites may not be reduced if their melting was limited by thick lithosphere.

ratios. The overlap of the natural refractory harzburgite data by the pMELTS model and the empirical model suggests that garnet-field melting is the primary driver of reduction in refractory low-f_{O2} ridge peridotites.

Magma and mantle f_{O2} through time

The temporal evolution of mantle f_{O2} is a matter of active debate. On the basis of vanadium partitioning, Archaean basalts[5], their residues[6,7] and komatiites[8] seem to record the same f_{O2} as modern MORB. By contrast, recent work on komatiites and modern plume/hotspot-generated picrites has suggested that the mantle has steadily evolved to be more oxidized since the Archaean, with the potential to generate the Great Oxidation Event in Earth's atmosphere about 2.5 billion years ago[10]. Our model can reconcile this discrepancy without the need to invoke a change in the bulk $Fe^{3+}/\Sigma Fe$ ratio of the mantle since the Archaean.

Although we have thus far focused on the f_{O2} of the residue, the low f_{O2} during hot, garnet-field melting has important implications for the f_{O2} of erupted lavas throughout Earth's history. Predictions about the f_{O2} of melts must be approached with caution. Although model melts and solid residues follow qualitatively similar f_{O2} paths, neither our model nor pMELTS force f_{O2} equilibrium between instantaneous melts and their solid residues, a requirement during near-fractional melting (Methods and Extended Data Fig. 10). Aggregated polybaric melts need not be in f_{O2} equilibrium with the last residues at the top of the melting column, but aggregated melts should record f_{O2} within the range spanned by the residues that produced them. Figure 4 illustrates the connection between f_{O2} of residues and aggregated near-fractional melts in modern and ancient settings.

At modern ridges, melting occurs only in the spinel field, in which potential temperature does not have a large effect on residue f_{O2} (Figs. 2a,b and 4b); here we expect residues, instantaneous melts and aggregated melts to all record similar f_{O2}, consistent with observations at modern ridges[2,25]. Similarly, we would expect most Archaean basalts—residues of ancient melting with higher average potential temperature but still melting predominantly in the spinel field—to record f_{O2} similar to modern MORB, as observed[5].

Some modern ocean island basalts (OIBs) show evidence for melting at high potential temperature in the garnet field, but in these settings, melting stops at high pressure and low F owing to thick overlying oceanic lithosphere (Fig. 4c). Thus, melting does not proceed shallowly enough to produce highly reduced residues or melts. Instead, OIBs are aggregated from melts generated near the garnet-field f_{O2} maximum and our modelling indicates that such melts—generated at low F and about 3–5 GPa by high-T_p mantle plumes—may be relatively oxidized (Figs. 2b and 4c). Indeed, some modern OIBs, rather than being particularly reduced, record conditions more oxidizing than MORB[56]. Alternatively, variations in f_{O2} recorded by OIBs may be compositional in nature[56–58].

By contrast, Archaean komatiites have geochemical and petrological signatures consistent with high extents of melting (high F) at high T_p in the garnet field and, critically, continuing to shallow pressure[59,60]. Our model predicts that komatiite petrogenesis initiating at pressures near the garnet-field f_{O2} maximum should lead to ultralow-f_{O2} residues and instantaneous melts (Fig. 4d) in the shallow portions of the melting column (Extended Data Fig. 10). This could potentially lead to a temporal trend in aggregated komatiite melt f_{O2} (ref. 10) at constant mantle $Fe^{3+}/\Sigma Fe$ ratio simply because of secular mantle cooling[48] and progressively

less reduction of the residue during garnet-field melting. We emphasize, however, that aggregated melts accumulate from a wide range of melt f_{O2} values—including more oxidizing melts from deeper in the melting column near the high-pressure f_{O2} maximum. Thus, Archaean melts (for example, refs. 61–63) need not be as reduced as the most refractory residues (Fig. 4d and Extended Data Fig. 10). Despite the uncertainty of our modelled liquid f_{O2} values, a robust implication is that lowering of average mantle potential temperatures with time[48] will result in proportionately less melt generation in the presence of garnet and fewer ultrareduced mantle residues. If melts generated much deeper than the garnet field f_{O2} maximum can be extracted and erupted, this presents an alternative mechanism, distinct from what we propose here, to generate low $Fe^{3+}/\Sigma Fe$, low f_{O2}, komatiitic melts at high pressure[49].

Although melt aggregation and focusing beneath ridges and a bias towards fertile sources may obscure heterogeneity in the basalt record[2,5], the refractory peridotites at the Gakkel Ridge and SWIR preserve ancient mantle that melted to high extents within the garnet stability field, leaving behind a highly reduced residue. These rafts of refractory, low and ultralow f_{O2} mantle contribute little to modern ridge volcanism. However, they indicate that high-F melting probably played an important role in ancient melt production, providing a mechanism for the generation of low-f_{O2} komatiites—but not necessarily basalts—without secular evolution of ambient mantle $Fe^{3+}/\Sigma Fe$ ratios through time.

Online content

Any methods, additional references, Nature Portfolio reporting summaries, source data, extended data, supplementary information, acknowledgements, peer review information; details of author contributions and competing interests; and statements of data and code availability are available at https://doi.org/10.1038/s41586-024-07603-w.

1. Bryndzia, L. T. & Wood, B. J. Oxygen thermobarometry of abyssal spinel peridotites: the redox state and C-O-H volatile composition of the Earth's sub-oceanic upper mantle. *Am. J. Sci.* **290**, 1093–1116 (1990).
2. Birner, S. K., Cottrell, E., Warren, J. M., Kelley, K. A. & Davis, F. A. Peridotites and basalts reveal broad congruence between two independent records of mantle f_{O2} despite local redox heterogeneity. *Earth Planet. Sci. Lett.* **494**, 172–189 (2018).
3. Cottrell, E. et al. in *Magma Redox Geochemistry* (eds Moretti, R. & Neuville, D. R.) Ch. 3 (American Geophysical Union, 2022).
4. Frost, D. J. & McCammon, C. A. The redox state of Earth's mantle. *Annu. Rev. Earth Planet. Sci.* **36**, 389–420 (2008).
5. Anser Li, Z. X. & Aeolus Lee, C. T. The constancy of upper mantle fO_2 through time inferred from V/Sc ratios in basalts. *Earth Planet. Sci. Lett.* **228**, 483–493 (2004).
6. Canil, D. Vanadium in peridotites, mantle redox and tectonic environments: Archean to present. *Earth Planet. Sci. Lett.* **195**, 75–90 (2002).
7. Lee, C.-T. A., Brandon, A. D. & Norman, M. Vanadium in peridotites as a proxy for paleo-fO_2 during partial melting: prospects, limitations, and implications. *Geochim. Cosmochim. Acta* **67**, 3045–3064 (2003).
8. Canil, D. Vanadium partitioning and the oxidation state of Archaean komatiite magmas. *Nature* **389**, 23–26 (1997).
9. Aulbach, S. & Stagno, V. Evidence for a reducing Archean ambient mantle and its effects on the carbon cycle. *Geology* **44**, 751–754 (2016).
10. Nicklas, R. W. et al. Secular mantle oxidation across the Archean-Proterozoic boundary: evidence from V partitioning in komatiites and picrites. *Geochim. Cosmochim. Acta* **250**, 49–75 (2019).
11. Stagno, V., Ojwang, D. O., McCammon, C. A. & Frost, D. J. The oxidation state of the mantle and the extraction of carbon from Earth's interior. *Nature* **493**, 84–88 (2013).
12. Wood, B. J., Bryndzia, L. T. & Johnson, K. E. Mantle oxidation state and its relationship to tectonic environment and fluid speciation. *Science* **248**, 337–345 (1990).
13. Stolper, D. A. & Bucholz, C. E. Neoproterozoic to early Phanerozoic rise in island arc redox state due to deep ocean oxygenation and increased marine sulfate levels. *Proc. Natl Acad. Sci. USA* **116**, 8746–8755 (2019).
14. Bucholz, C. E., Stolper, E. M., Eiler, J. M. & Breaks, F. W. A comparison of oxygen fugacities of strongly peraluminous granites across the Archean–Proterozoic boundary. *J. Petrol.* **59**, 2123–2156 (2018).
15. Zhang, H. L., Cottrell, E., Solheid, P., Kelley, K. A. & Hirschmann, M. M. Determination of $Fe^{3+}/\Sigma Fe$ of XANES basaltic glass standards by Mössbauer spectroscopy and its application to the oxidation state of iron in MORB. *Chem. Geol.* **479**, 166–175 (2018).
16. O'Neill, H. S. C., Berry, A. J. & Mallmann, G. The oxidation state of iron in Mid-Ocean Ridge Basaltic (MORB) glasses: implications for their petrogenesis and oxygen fugacities. *Earth Planet. Sci. Lett.* **504**, 152–162 (2018).
17. Cottrell, E. & Kelley, K. A. The oxidation state of Fe in MORB glasses and the oxygen fugacity of the upper mantle. *Earth Planet. Sci. Lett.* **305**, 270–282 (2011).
18. Kelemen, P. B., Hirth, G., Shimizu, N., Spiegelman, M. & Dick, H. J. A review of melt migration processes in the adiabatically upwelling mantle beneath oceanic spreading ridges. *Phil. Trans. R. Soc. A Math. Phys. Eng. Sci.* **355**, 283–318 (1997).
19. Warren, J. M. Global variations in abyssal peridotite compositions. *Lithos* **248–251**, 193–219 (2016).
20. Voigt, M. & von der Handt, A. Influence of subsolidus processes on the chromium number in spinel in ultramafic rocks. *Contrib. Mineral. Petrol.* **162**, 675–689 (2011).
21. Andreani, M., Mével, C., Boullier, A.-M. & Escartín, J. Dynamic control on serpentine crystallization in veins: constraints on hydration processes in oceanic peridotites. *Geochem. Geophys. Geosyst.* **8**, Q02012 (2007).
22. Birner, S. K., Warren, J. M., Cottrell, E. & Davis, F. A. Hydrothermal alteration of seafloor peridotites does not influence oxygen fugacity recorded by spinel oxybarometry. *Geology* **44**, 535–538 (2016).
23. Sorbadere, F. et al. The behaviour of ferric iron during partial melting of peridotite. *Geochim. Cosmochim. Acta* **239**, 235–254 (2018).
24. Davis, F. A. & Cottrell, E. Experimental investigation of basalt and peridotite oxybarometers: implications for spinel thermodynamic models and Fe^{3+} compatibility during generation of upper mantle melts. *Am. Mineral.* **103**, 1056–1067 (2018).
25. Birner, S. K., Cottrell, E., Warren, J. M., Kelley, K. A. & Davis, F. A. Melt addition to mid-ocean ridge peridotites increases spinel Cr# with no significant effect on recorded oxygen fugacity. *Earth Planet. Sci. Lett.* **566**, 116951 (2021).
26. Salters, V. J. M. & Dick, H. J. B. Mineralogy of the mid-ocean-ridge basalt source from neodymium isotopic composition of abyssal peridotites. *Nature* **418**, 68–72 (2002).
27. Shorttle, O., Maclennan, J. & Lambart, S. Quantifying lithological variability in the mantle. *Earth Planet. Sci. Lett.* **395**, 24–40 (2014).
28. Cipriani, A., Brueckner, H. K., Bonatti, E. & Brunelli, D. Oceanic crust generated by elusive parents: Sr and Nd isotopes in basalt-peridotite pairs from the Mid-Atlantic Ridge. *Geology* **32**, 657–660 (2004).
29. Warren, J. M., Shimizu, N., Sakaguchi, C., Dick, H. J. B. & Nakamura, E. An assessment of upper mantle heterogeneity based on abyssal peridotite isotopic compositions. *J. Geophys. Res. Solid Earth* **114**, B12203 (2009).
30. Mallick, S., Dick, H. J. B., Sachi-Kocher, A. & Salters, V. J. M. Isotope and trace element insights into heterogeneity of subridge mantle. *Geochem. Geophys. Geosyst.* **15**, 2438–2453 (2014).
31. Liu, C.-Z. et al. Ancient, highly heterogeneous mantle beneath Gakkel ridge, Arctic Ocean. *Nature* **452**, 311–316 (2008).
32. D'Errico, M. E., Warren, J. M. & Godard, M. Evidence for chemically heterogeneous Arctic mantle beneath the Gakkel Ridge. *Geochim. Cosmochim. Acta* **174**, 291–312 (2016).
33. Liu, C. et al. Archean cratonic mantle recycled at a mid-ocean ridge. *Sci. Adv.* **8**, eabn6749 (2022).
34. Seyler, M., Cannat, M. & Mével, C. Evidence for major-element heterogeneity in the mantle source of abyssal peridotites from the Southwest Indian Ridge (52° to 68°E). *Geochem. Geophys. Geosyst.* **4**, 9101 (2003).
35. Byerly, B. L. & Lassiter, J. C. Isotopically ultradepleted domains in the convecting upper mantle: implications for MORB petrogenesis. *Geology* **42**, 203–206 (2014).
36. Wood, B. J. & Virgo, D. Upper mantle oxidation state: ferric iron contents of lherzolite spinels by ^{57}Fe Mössbauer spectroscopy and resultant oxygen fugacities. *Geochim. Cosmochim. Acta* **53**, 1277–1291 (1989).
37. Davis, F. A., Cottrell, E., Birner, S. K., Warren, J. M. & Lopez, O. G. Revisiting the electron microprobe method of spinel-olivine-orthopyroxene oxybarometry applied to spinel peridotites. *Am. Mineral.* **102**, 421–435 (2017).
38. Dick, H. J. B. & Natland, J. H. in *Proceedings of the Ocean Drilling Program, Scientific Results* Vol. 147 (eds Mével, C., Gillis, K. M., Allan, J. F. & Meyer, P. S.) 103–134 (Ocean Drilling Program, 1996).
39. Hesse, K. T., Gose, J., Stalder, R. & Schmädicke, E. Water in orthopyroxene from abyssal spinel peridotites of the East Pacific Rise (ODP Leg 147: Hess Deep). *Lithos* **232**, 23–34 (2015).
40. Smith, D. K., Schouten, H., Turner, R. P. & Klein, E. M. The evolution of seafloor spreading behind the tip of the westward propagating Cocos-Nazca spreading center. *Geochem. Geophys. Geosyst.* **21**, e2020GC008957 (2020).
41. Bown, J. W. & White, R. S. Variation with spreading rate of oceanic crustal thickness and geochemistry. *Earth Planet. Sci. Lett.* **121**, 435–449 (1994).
42. Bézos, A. & Humler, E. The $Fe^{3+}/\Sigma Fe$ ratios of MORB glasses and their implications for mantle melting. *Geochim. Cosmochim. Acta* **69**, 711–725 (2005).
43. Jokat, W. et al. Geophysical evidence for reduced melt production on the Arctic ultraslow Gakkel mid-ocean ridge. *Nature* **423**, 962–965 (2003).
44. Dick, H. J. B., Lin, J. & Schouten, H. An ultraslow-spreading class of ocean ridge. *Nature* **426**, 405–412 (2003).
45. Cannat, M. How thick is the magmatic crust at slow spreading oceanic ridges? *J. Geophys. Res. Solid Earth* **101**, 2847–2857 (1996).
46. Stracke, A. et al. Abyssal peridotite Hf isotopes identify extreme mantle depletion. *Earth Planet. Sci. Lett.* **308**, 359–368 (2011).
47. Lassiter, J. C., Byerly, B. L., Snow, J. E. & Hellebrand, E. Constraints from Os-isotope variations on the origin of Lena Trough abyssal peridotites and implications for the composition and evolution of the depleted upper mantle. *Earth Planet. Sci. Lett.* **403**, 178–187 (2014).
48. Herzberg, C., Condie, K. & Korenaga, J. Thermal history of the Earth and its petrological expression. *Earth Planet. Sci. Lett.* **292**, 79–88 (2010).
49. Gaillard, F., Scaillet, B., Pichavant, M. & Iacono-Marziano, G. The redox geodynamics linking basalts and their mantle sources through space and time. *Chem. Geol.* **418**, 217–233 (2015).
50. Ghiorso, M. S., Hirschmann, M. M., Reiners, P. W. & Kress, V. C. The pMELTS: a revision of MELTS for improved calculation of phase relations and major element partitioning related to partial melting of the mantle to 3 GPa. *Geochem. Geophys. Geosyst.* **3**, 1–35 (2002).
51. Stolper, E. M., Shorttle, O., Antoshechkina, P. M. & Asimow, P. D. The effects of solid-solid phase equilibria on the oxygen fugacity of the upper mantle. *Am. Mineral.* **105**, 1445–1471 (2020).

52. Davis, F. A. & Cottrell, E. Partitioning of Fe_2O_3 in peridotite partial melting experiments over a range of oxygen fugacities elucidates ferric iron systematics in mid-ocean ridge basalts and ferric iron content of the upper mantle. *Contrib. Mineral. Petrol.* **176**, 67 (2021).
53. Gaetani, G. A. The behavior of $Fe^{3+}/\sum Fe$ during partial melting of spinel lherzolite. *Geochim. Cosmochim. Acta* **185**, 64–77 (2016).
54. Jennings, E. S. & Holland, T. J. B. A simple thermodynamic model for melting of peridotite in the system NCFMASOCr. *J. Petrol.* **56**, 869–892 (2015).
55. Gudmundsson, G. & Wood, B. J. Experimental tests of garnet peridotite oxygen barometry. *Contrib. Mineral. Petrol.* **119**, 56–67 (1995).
56. Moussallam, Y. et al. Mantle plumes are oxidised. *Earth Planet. Sci. Lett.* **527**, 115798 (2019).
57. Shorttle, O. et al. Fe-XANES analyses of Reykjanes Ridge basalts: implications for oceanic crust's role in the solid Earth oxygen cycle. *Earth Planet. Sci. Lett.* **427**, 272–285 (2015).
58. Brounce, M., Stolper, E. & Eiler, J. The mantle source of basalts from Reunion Island is not more oxidized than the MORB source mantle. *Contrib. Mineral. Petrol.* **177**, 1–18 (2022).
59. Herzberg, C. Depth and degree of melting of komatiites. *J. Geophys. Res. Solid Earth* **97**, 4521–4540 (1992).
60. Arndt, N. T. & Lesher, C. M. in *Encyclopedia of Geology* 260–268 (Elsevier, 2004).
61. Berry, A. J., Danyushevsky, L. V., O'Neill, H. S. C., Newville, M. & Sutton, S. R. Oxidation state of iron in komatiitic melt inclusions indicates hot Archaean mantle. *Nature* **455**, 960–963 (2008).
62. Asafov, E. V. et al. Belingwe komatiites (2.7 Ga) originate from a plume with moderate water content, as inferred from inclusions in olivine. *Chem. Geol.* **478**, 39–59 (2018).
63. Sobolev, A. V. et al. Komatiites reveal a hydrous Archaean deep-mantle reservoir. *Nature* **531**, 628–632 (2016).

Methods

Major elements

We collected new mineral major element data for Hess Deep peridotites (spinel, olivine and orthopyroxene) and Gakkel Ridge peridotites (spinel only; olivine and orthopyroxene from ref. 32) through electron microprobe analysis at the Smithsonian Institution, following the procedures in refs. 2,37. For olivine, we analysed six points per sample, whereas for orthopyroxene, we analysed nine points along a transect perpendicular to exsolution, with a defocused beam, to determine average pyroxene composition before cooling. Data with totals <98.5 wt% or >101.5 wt% were discarded. For spinel, we measured three grains per sample and three points per grain. Instrument information, analytical conditions and data can be found in the EarthChem repository[64–67].

Oxygen fugacity

We calculated new f_{O2} data for the Gakkel Ridge and Hess Deep peridotites using the methodology and parameters reported in ref. 2. As calculation of f_{O2} depends most heavily on precise and accurate determination of ferric iron in spinel, we used the Cr#-based correction method in ref. 37, revised from ref. 36, to determine spinel $Fe^{3+}/\Sigma Fe$ ratios by microprobe. Raw $Fe^{3+}/\Sigma Fe$ values from stoichiometry were corrected using a set of 6–8 calibration spinel standards with $Fe^{3+}/\Sigma Fe$ ratios independently characterized by Mössbauer spectroscopy[36] (calibration spinel data for each session are reported in Supplementary Table 2). After applying this correction, oxides returning negative concentrations were corrected to 0 and analyses with oxide totals <98.0 wt% or >101.5 wt% were discarded.

Calculation of f_{O2} also depends on the pressure and temperature of last equilibration. As detailed in ref. 2, we used temperatures determined from olivine–spinel thermometry[68], as this geothermometer is reliant on the same Fe^{2+}/Mg^{2+} exchange as our oxybarometer. When we plot recorded f_{O2} values (for example, Fig. 1), we use a pressure of 0.6 GPa to be consistent with these recorded temperatures, using the ridge thermal structure parameterization in ref. 69. When we project natural peridotite f_{O2} data to source conditions (for example, Fig. 3), we use the iso-compositional + exchange reactions approach described in ref. 2. For the SWIR and Gakkel Ridge samples, we project to 1.25 GPa and 1,320 °C (the conditions of basalt extraction determined from SWIR samples[2]). These conditions were chosen from our T_p = 1,350 °C pMELTS model output (initial composition = depleted MORB mantle (DMM)) to match the estimated degree of melting of the Hess Deep peridotites (F = 17.5% (ref. 39)).

To calculate f_{O2}, we used the oxygen barometer formulation presented in ref. 37, based on phase equilibrium between olivine, orthopyroxene and spinel (equations (1a) and (1b)):

$$6Fe_2SiO_4(olv) + O_2 <-> 3Fe_2Si_2O_6(opx) + 2Fe_3O_4(spl) \quad (1a)$$

$$\begin{aligned}\log(f_{O2})_{P,T} &= \log f_{O2}\,(\mathrm{FFM}) - 6\log a_{Fe2SiO4} + 3\log a_{Fe2Si2O6} \\ &\quad + 2\log a_{Fe3O4} \\ &= \left[\frac{-24,222}{T} + 8.64 + \frac{0.0567P}{T}\right] - 12\log(1 - \mathrm{Mg\#^{olv}}) \\ &\quad - \frac{2,620}{T}(\mathrm{Mg\#^{olv}})^2 + 3\log(X_{Fe}^{M1}X_{Fe}^{M2})^{opx} + 2\log a_{Fe3O4}^{spl}\end{aligned} \quad (1b)$$

in which T is in kelvin, P is in bar and $\log f_{O2}$(FFM) represents the f_{O2} of an assemblage of pure fayalite, ferrosilite and magnetite[37].

When comparing with the QFM buffer, we use the formulation in ref. 70. When comparing with the formulation of FFM, we use the formulation in refs. 36,71, as described in ref. 37 (see the next section for further details related to use of the QFM and FFM buffers).

When comparing our data with the ridge peridotite f_{O2} dataset in ref. 1, we recalculate the f_{O2} values of ref. 1 from their reported major element data to maintain consistency with the methodology used for this study (see ref. 2 for details). Although ref. 1 reported relatively low f_{O2} values for their peridotites (between QFM-2 and QFM), the recalculated values fall primarily between QFM and QFM+1, consistent with the SWIR/Gakkel Ridge residual lherzolites reported in this study. This shift upwards results primarily from two factors: (1) the Nell–Wood spinel activity model[72] used in ref. 1 returns lower magnetite activity for a given spinel composition than the Sack–Ghiorso spinel activity model[73,74] used in ref. 37 (see ref. 75) and (2) the two-pyroxene thermometer used in ref. 1 returns higher temperatures than the spinel–olivine thermometer used in ref. 37.

We explored using olivine vanadium (V) concentrations as an f_{O2} proxy (for example, refs. 8,10) to corroborate our oxybarometry, but this technique is unsuitable for our samples for several reasons. First, we cannot disambiguate the competing effects from low f_{O2} (expected to drive V concentration in olivine up relative to the corresponding melt) and high-F melting (expected to drive V concentration in olivine down). Further, we do not have samples of the corresponding melts with which to calculate olivine–melt partition coefficients. Finally, partition coefficients for V during garnet-field melting are not well constrained, which has precluded application of the V oxybarometer in other studies (for example, ref. 7).

Choice of FFM versus QFM as reference buffer

Oxygen fugacity is typically reported relative to a solid buffer to minimize the effects of pressure and temperature. Although the f_{O2} of natural peridotite samples is traditionally reported relative to the QFM buffer (equations (2a) and (2b))[70], the FFM buffer (equations (3a) and (3b))[36,37,71] provides a better choice for interpreting models of peridotite evolution during adiabatic decompression[51]. Because the FFM buffer uses the same assemblage that is present in peridotite oxybarometry (olivine–orthopyroxene–spinel), adiabatic ascent of peridotite does not have a strong effect on f_{O2} relative to FFM. A residue with f_{O2} changing relative to QFM during ascent may not be recording an actual oxidative effect but rather the divergence of the QFM and FFM buffers in P–T space (Extended Data Fig. 2).

$$3Fe_2SiO_4(\mathrm{fayalite}) + O_2 <-> 3SiO_2(\mathrm{quartz}) + 2Fe_3O_4(\mathrm{magnetite}) \quad (2a)$$

$$\log f_{O2}\,(\mathrm{QFM}) = \left(\frac{-25,096.3}{T} + 8.735 + 0.11 \times \frac{P-1}{T}\right) \quad (2b)$$

$$\log f_{O2}, \Delta\mathrm{QFM} = \log f_{O2} - \log f_{O2}\,(\mathrm{QFM}) \quad (2c)$$

$$6Fe_2SiO_4(\mathrm{fayalite}) + O_2 <-> 3Fe_2Si_2O_6(\mathrm{ferrosilite}) + 2Fe_3O_4(\mathrm{magnetite}) \quad (3a)$$

$$\log f_{O2}\,(\mathrm{FFM}) = \left(\frac{-24,222}{T} + 8.64 + 0.0567 \times \frac{P-1}{T}\right) \quad (3b)$$

$$\log f_{O2}, \Delta\mathrm{FFM} = \log f_{O2} - \log f_{O2}\,(\mathrm{FFM}) \quad (3c)$$

The formulation for FFM is simply the first three terms of the spinel oxybarometer (equation (1b)), as it represents the Gibbs free energy of the reaction of the pure phases at pressure and temperature. Divergence of the natural assemblage from the FFM buffer is then because of only the changes in mineral activities:

$$\log f_{O2}, \Delta\mathrm{FFM} = 2\log a_{Fe3O4} + 3\log a_{Fe2Si2O6} - 6\log a_{Fe2SiO4} \quad (4)$$

For all of the above equations, T is in kelvin and P is in bar.

When we plot only natural sample data (for example, Fig. 1), we plot data relative to QFM to maintain straightforward comparisons with literature data, but we include a secondary axis showing approximate

FFM values. Although offsets between ΔQFM and ΔFFM values are not constant (the buffers are a function of temperature, which varies between samples), the changes in relative position between samples are imperceptible on the scale of our plots (1σ for variation in offset values = 0.02 log units). Thus, the difference between ΔQFM and ΔFFM values can be approximated as a constant offset of 0.37 log units. When we plot modelling results (for example, Figs. 2 and 3), we use the FFM buffer to eliminate misleading trends associated with the divergence of the two buffers.

Statistics

To demonstrate that the refractory SWIR/Gakkel Ridge samples record much lower f_{O2} than the residual SWIR/Gakkel Ridge samples and/or the global non-melt-influenced residual peridotite dataset, we performed the Mann–Whitney *U* test on our datasets, as described in detail in the Supplementary Methods. In all three cases, we rejected the null hypothesis that the distributions underlying the two populations are the same, supporting instead the alternative hypothesis that the SWIR/Gakkel Ridge refractory samples record lower f_{O2} than residual samples ($P < 0.01$ for all tests).

pMELTS modelling

To investigate the geochemical and thermodynamic histories of our peridotites, we applied pMELTS modelling through the alphaMELTS1 interface[50,76]. All models are isentropic decompression models beginning at 4 GPa. Models are not f_{O2}-buffered, to allow f_{O2} to evolve during decompression. Each set of models is described below.

a. Evolution of DMM mantle[77] at T_p ranging from 1,350 °C to 1,550 °C (ref. 69). The initial bulk $Fe^{3+}/\Sigma Fe$ ratio was set to 0.03 for all runs[78]. We ran four iterations, each suppressing/allowing different phases.
   - Melting + garnet suppressed
   - Melting suppressed, garnet allowed
   - Melting allowed, garnet suppressed
   - Melting + garnet allowed
b. Evolution of refractory bulk compositions (representing mantle that has undergone previous melt-extraction events) along a 1,350 °C adiabat. These refractory residues have previously undergone 10–35% melting along the 1,550 °C adiabat output from part (a).

pMELTS model outputs can be reproduced using the code and parameters reported in Supplementary Table 3 and the Supplementary Methods. Output tables are tabulated in Supplementary Table 4 and plotted in Extended Data Fig. 4.

Treatment of f_{O2} in pMELTS. f_{O2} values in pMELTS are calculated in two distinct manners. Below the solidus, the activities of the solid mineral phases are used to calculate f_{O2} from oxybarometry. However, when melt is present in the system, pMELTS defaults to calculating the f_{O2} of the system based on the composition of the melt phase, using the formulation of ref. 79. If the 'alternative-fO2' flag is set in pMELTS, then the f_{O2} output will instead use the activity of the solid mineral phases, as is done in the subsolidus case, even when melt is present. Notably, these two methods of calculating f_{O2} above the solidus are not consistent with one another—whereas the compositions of the model minerals and melt are identical regardless of which f_{O2} method is specified, the f_{O2} output by alphaMELTS may differ by several log units, depending on the chosen method[24,53].

Furthermore, when using the 'alternative-fO2' option, pMELTS substantially underestimates f_{O2} compared with calculating f_{O2} from the same model mineral compositions using the empirical spinel oxybarometer[36,37] that we use for calculating f_{O2} of our natural samples (see also Extended Data Fig. 10). Overall, the spinel oxybarometer returns f_{O2} values approximately 1.2 log units higher than the pMELTS model. This offset is approximately constant across our modelled decompression paths and is primarily because of differences in estimates for the activity of the fayalite component within olivine ($\Delta_{empirical\text{-}pMELTS}$ = +1.8 log units) with smaller contributions from the Gibbs free energy of reaction of the pure phases ($\Delta_{empirical\text{-}pMELTS}$ = −1.1 log units) and the activity of ferrosilite within orthopyroxene ($\Delta_{empirical\text{-}pMELTS}$ = +0.5 log units). The activity of magnetite in spinel is the same between the two methods, as the empirical spinel oxybarometer uses the pMELTS spinel activity model for calculating magnetite activity. Because the empirical spinel oxybarometer returns values for mid-ocean ridge peridotites that are consistent with f_{O2} determined experimentally[24] as well as with MORBs[2], we conclude that the empirical spinel oxybarometer is more accurate, in terms of the magnitude of f_{O2}, than is the pMELTS 'alternative-fO2' model.

To avoid these issues and maintain consistency with the calculation of f_{O2} for our natural samples and the empirical model, we recalculate pMELTS f_{O2} values using the pMELTS mineral compositions and the empirical spinel oxybarometer formulation. This allows us to make direct comparisons between pMELTS model results, our empirical model results and natural samples. We show in Fig. 3 that this recalculation results in good agreement between pMELTS f_{O2} values and natural sample f_{O2} values along modern geotherms, when natural samples are projected to source conditions.

Empirical modelling

To investigate changes in oxygen fugacity during garnet-field and spinel-field melting, we developed an empirical mass-balance model to track element partitioning between phases. The model functions by solving a nonlinear system of equations at each pressure step. The variables in the system of equations are exchange reactions that allow mineral compositions to vary (while holding bulk composition of the system constant) and the constraints are partitioning relationships determined from natural samples and experiments. Key aspects of our empirical model are described below, with further details and steps for reproducing the calculations provided in the Supplementary Methods. Our model outputs (Extended Data Fig. 5 and Supplementary Table 5) can be reproduced using the provided code and parameters (CodeOcean, https://doi.org/10.24433/CO.9619937.v1).

Phases and components. The model contains six phases (olivine, orthopyroxene, clinopyroxene, spinel, garnet and melt) and seven oxide components (CaO, FeO, MgO, Al_2O_3, Cr_2O_3, Fe_2O_3 and SiO_2). Each solid phase maintains stoichiometry during modelled reactions. Phases, stoichiometry and included oxide components are listed in Extended Data Table 1. We use the composition of DMM[77] projected to the garnet stability field (see Supplementary Methods). To model the decompression of a peridotite residue along an adiabat, our model calculates *T* and *F* at each pressure step using the equations in ref. 80, as described in the Supplementary Methods.

Olivine, orthopyroxene and clinopyroxene are present in all model runs. Liquid is present at temperatures above the solidus (see Supplementary Methods). Garnet is present at pressures higher than garnet-out (2.8 GPa).

Although in the Earth spinel is present only in peridotites over a limited pressure range (about 0.5–3.0 GPa), our model contains small amounts of spinel across all pressures. This is also true in pMELTS, but the motivation to maintain spinel as a ubiquitous phase in our empirical model is different. Our modelling relies on a combination of mineral/melt and intermineral partition coefficients. The Fe^{3+} partition coefficient that is best constrained by experiments is the spinel/melt partition coefficient[24,52]. We calculate Fe^{3+} in the solid phases through intermineral partition coefficients and connect these to the melt phase by the experimentally determined spinel/melt partition coefficient. Maintaining a small amount of spinel in the system allows us to use spinel as an intermediate phase for determining partitioning constraints and maintain a consistent method of connecting Fe^{3+} in the melt to Fe^{3+} in the residue, even in the garnet field. The temperature dependence

of the experimentally determined spinel/melt partition coefficient for Fe_2O_3 (ref. 52) imparts a temperature dependence on the bulk Fe_2O_3 partition coefficient that is a distinct difference between the empirical model and pMELTS.

When using the phrase 'spinel stability field', we use it to refer only to the pressure range in which spinel is present at low pressures in the absence of garnet (<2.8 GPa). We use 'garnet stability field' to refer to pressures greater than garnet-out, at which garnet is actively reacting to form spinel and pyroxene (2.8–3.0 GPa) or at higher pressures, at which spinel is left in the solid assemblage in trace quantities to aid calculation of the Fe^{3+} distribution between phases and calculate f_{O2} in the garnet field (>3 GPa; spinel mode = 0.05 wt%).

The pMELTS model that we compare with our empirical model also incorporates spinel across all pressure ranges, although for a different reason. In pMELTS, spinel is present at high pressures because it is the only solid phase that can incorporate Cr (there are no Cr-bearing components in pyroxenes and garnet in pMELTS) and so any bulk composition below its solidus or containing more Cr than can be dissolved in the liquid must have spinel present as a phase. Owing to this constraint, pMELTS produces approximately 1.2 wt% metastable spinel throughout the garnet stability field. In our model, because both garnet and the pyroxenes incorporate Cr, we maintain a much smaller amount of spinel and thus more faithfully approach a 'true' garnet-field assemblage than pMELTS. Our residues contain 0.05 wt% spinel at 4 GPa. We assessed the effect of 'excess' spinel in the garnet stability field by adding spinel back into the garnet-field residue in our empirical model until we reached the 1.2 wt% of spinel found in the pMELTS model. We found that this extra spinel decreases residue f_{O2} by about 1 log unit, which is approximately the difference in f_{O2} between our model and pMELTS in the garnet field below the solidus at any given potential temperature (Fig. 2). This suggests that the lower f_{O2} reported in the garnet field by the pMELTS model relative to our empirical model may be because of the higher spinel content that pMELTS must maintain to host the entirety of the system's Cr content. Thus, relative to pMELTS, our empirical model may better predict the magnitude of the decrease in f_{O2} across the garnet-to-spinel transition.

Exchange/partitioning constraints. The compositional constraints and exchange reactions that the model fulfils at each pressure step are reported in Extended Data Table 2. For a given assemblage, the number of partitioning equations (constraints) equals the number of exchange reactions (variables). From an initial composition of each phase in the system, the model uses an optimization routine to vary the extent of each exchange reaction to fulfil the necessary constraints for the new mineral compositions.

Garnet-out reactions. To model the decompression of a peridotite residue from the garnet field to the spinel field, we use four subsolidus garnet-out reactions (Extended Data Table 3), adapted from equations in ref. 51. At each step, the amount of garnet removed is calculated from the total garnet present and the remaining pressure range before garnet-out:

$$\text{Mass\_garnet\_to\_remove} = \text{Mass\_garnet}/(\text{remaining\_gt\_field\_}P\text{\_range}/P\text{\_step\_size})$$

The removed garnet mass is divided among the four garnet-out reactions, as reported in Extended Data Table 3.

Melting reactions. To model near-fractional melting of a peridotite residue, we use experimentally determined garnet-field and spinel-field melting reactions[81,82] to track incremental and aggregated liquid phases. We use experimental data from the Library of Experimental Phase Relations (LEPR)[83] to determine an empirical relationship between Tschermak's pyroxene components and spinel Cr#, as described in the Supplementary Methods.

Calculation of liquid f_{O2}

Neither pMELTS nor our empirical model requires that instantaneous liquids be produced in f_{O2} equilibrium with their residues, although this is probably true in nature. We use f_{O2}–composition relationships to determine the f_{O2} recorded by our modelled liquids and assess the agreement with modelled residue f_{O2} as calculated using spinel oxybarometry. No model relating melt composition to f_{O2} based on experimental data is well suited for our modelled melts, which are unusual in composition, both because of our empirical model's exclusion of minor elements such as K_2O, Na_2O, TiO_2 and P_2O_5 and because of high MgO and FeO values in garnet-field melts. To choose the best model, we replicated the f_{O2} parameterization analysis in ref. 3 on subsets of published controlled-atmosphere experiments that are most like our modelled liquids. The algorithm in ref. 84 for composition offers superior predictive capability: compositions that lack Na, K, P and Ti return standard error between calculated and measured furnace f_{O2} equal to 0.26 log units (compared with 0.34 and 0.47 log units for ref. 16 and ref. 79, respectively) and f_{O2} of modelled liquids with high MgO and FeO (such as those in equilibrium with garnet) are more accurate. In Extended Data Fig. 10, we show liquid f_{O2} values calculated from pMELTS and our empirical model output using ref. 84. We apply the pressure term of ref. 79, which accurately models changes in $Fe^{3+}/\Sigma Fe$ as a function of pressure from 1–4 GPa (refs. 85,86). For comparison, we show results using the formulation of ref. 87, which modifies and expands the compositional treatment of ref. 84 and applies a pressure term derived from ref. 88.

Data availability

All new data and metadata necessary to reproduce our results are available through EarthChem (https://www.earthchem.org/) at https://doi.org/10.60520/IEDA/113225, using microprobe methods for spinel (https://doi.org/10.60520/IEDA/113226), olivine (https://doi.org/10.60520/IEDA/113227) and orthopyroxene (https://doi.org/10.60520/IEDA/113228).

Code availability

pMELTS modelling in this manuscript can be reproduced using alphaMELTS, which is publicly available at https://magmasource.caltech.edu/alphamelts/. We include instructions for reproducing our pMELTS modelling results in Methods and all input files and output data are included in the Supplementary Information. Empirical modelling can be reproduced using the provided code (CodeOcean, https://doi.org/10.24433/CO.9619937.v1) and parameters, and our output tables are tabulated in the Supplementary Information.

64. Birner, S. K., Cottrell, E., Davis, F. A. & Warren, J. M. Major elements EMPA method for pyroxene, Version 1.0. Interdisciplinary Earth Data Alliance (IEDA) https://doi.org/10.60520/IEDA/113228 (2024).
65. Birner, S. K., Cottrell, E., Davis, F. A. & Warren, J. M. Major elements EMPA method for olivine, Version 1.0. Interdisciplinary Earth Data Alliance (IEDA) https://doi.org/10.60520/IEDA/113227 (2024).
66. Birner, S. K., Cottrell, E., Davis, F. A. & Warren, J. M. Major elements EMPA method for spinel with secondary standards, Version 1.0. Interdisciplinary Earth Data Alliance (IEDA) https://doi.org/10.60520/IEDA/113226 (2024).
67. Birner, S. K., Cottrell, E., Davis, F. A. & Warren, J. M. Spinel oxybarometry of abyssal peridotites from the Gakkel Ridge and Hess Deep, Version 1.0. Interdisciplinary Earth Data Alliance (IEDA) https://doi.org/10.60520/IEDA/113225 (2024).
68. Li, J., Kornprobst, J., Vielzeuf, D. & Fabriès, J. An improved experimental calibration of the olivine-spinel geothermometer. *Chin. J. Geochem.* **14**, 68–77 (1995).
69. Montési, L. G. J. & Behn, M. D. Mantle flow and melting underneath oblique and ultraslow mid-ocean ridges. *Geophys. Res. Lett.* **34**, L24307 (2007).
70. Frost, B. R. in *Oxide Minerals: Petrologic and Magnetic Significance* (ed. Lindsley, D. H.) 1–9 (De Gruyter, 1991).

71. Mattioli, G. S. & Wood, B. J. Magnetite activities across the $MgAl_2O_4$-Fe_3O_4 spinel join, with application to thermobarometric estimates of upper mantle oxygen fugacity. *Contrib. Mineral. Petrol.* **98**, 148–162 (1988).
72. Nell, J. & Wood, B. J. Thermodynamic properties in a multicomponent solid solution involving cation disorder; Fe_3O_4-$MgFe_2O_4$-$FeAl_2O_4$-$MgAl_2O_4$ spinels. *Am. Mineral.* **74**, 1000–1015 (1989).
73. Sack, R. O. & Ghiorso, M. S. An internally consistent model for the thermodynamic properties of Fe–Mg–titanomagnetite–aluminate spinels. *Contrib. Mineral. Petrol.* **106**, 474–505 (1991).
74. Sack, R. O. & Ghiorso, M. S. Chromian spinels as petrogenetic indicators: thermodynamics and petrological applications. *Am. Mineral.* **76**, 827–847 (1991).
75. Birner, S. K. et al. Forearc peridotites from Tonga record heterogeneous oxidation of the mantle following subduction initiation. *J. Petrol.* **58**, 1755–1780 (2017).
76. Smith, P. M. & Asimow, P. D. Adiabat_1ph: a new public front-end to the MELTS, pMELTS, and pHMELTS models. *Geochem. Geophys. Geosyst.* **6**, Q02004 (2005).
77. Workman, R. K. & Hart, S. R. Major and trace element composition of the depleted MORB mantle (DMM). *Earth Planet. Sci. Lett.* **231**, 53–72 (2005).
78. Canil, D. et al. Ferric iron in peridotites and mantle oxidation states. *Earth Planet. Sci. Lett.* **123**, 205–220 (1994).
79. Kress, V. C. & Carmichael, I. S. E. The compressibility of silicate liquids containing Fe_2O_3 and the effect of composition, temperature, oxygen fugacity and pressure on their redox states. *Contrib. Mineral. Petrol.* **108**, 82–92 (1991).
80. Langmuir, C. H., Klein, E. M. & Plank, T. Petrological systematics of Mid-Ocean Ridge basalts: constraints on melt generation beneath ocean ridges. *Geophys. Monogr.* **71**, 183–280 (1992).
81. Walter, M. J. Melting of garnet peridotite and the origin of komatiite and depleted lithosphere. *J. Petrol.* **39**, 29–60 (1998).
82. Falloon, T. J., Green, D. H., Danyushevsky, L. V. & McNeill, A. W. The composition of near-solidus partial melts of fertile peridotite at 1 and 1·5 GPa: implications for the petrogenesis of MORB. *J. Petrol.* **49**, 591–613 (2008).
Q18
83. Hirschmann, M. M. et al. Library of Experimental Phase Relations (LEPR): a database and Web portal for experimental magmatic phase equilibria data. *Geochem. Geophys. Geosyst.* **9**, Q03011 (2008).
84. Borisov, A., Behrens, H. & Holtz, F. Ferric/ferrous ratio in silicate melts: a new model for 1 atm data with special emphasis on the effects of melt composition. *Contrib. Mineral. Petrol.* **173**, 98 (2018).
85. O'Neill, H. S. C. et al. An experimental determination of the effect of pressure on the $Fe^{3+}/\Sigma Fe$ ratio of an anhydrous silicate melt to 3.0 GPa. *Am. Mineral.* **91**, 404–412 (2006).
86. Zhang, H. L., Hirschmann, M. M., Cottrell, E. & Withers, A. C. Effect of pressure on $Fe^{3+}/\Sigma Fe$ ratio in a mafic magma and consequences for magma ocean redox gradients. *Geochim. Cosmochim. Acta* **204**, 83–103 (2017).
87. Hirschmann, M. M. Magma oceans, iron and chromium redox, and the origin of comparatively oxidized planetary mantles. *Geochim. Cosmochim. Acta* **328**, 221–241 (2022).
88. Deng, J., Du, Z., Karki, B. B., Ghosh, D. B. & Lee, K. K. M. A magma ocean origin to divergent redox evolutions of rocky planetary bodies and early atmospheres. *Nat. Commun.* **11**, 2007 (2020).
89. Witt-Eickschen, G. & O'Neill, H. S. C. The effect of temperature on the equilibrium distribution of trace elements between clinopyroxene, orthopyroxene, olivine and spinel in upper mantle peridotite. *Chem. Geol.* **221**, 65–101 (2005).
90. Canil, D. & O'Neill, H. S. C. Distribution of ferric iron in some upper-mantle assemblages. *J. Petrol.* **37**, 609–635 (1996).
91. Dyar, M. D., Mcguire, A. V. & Harrell, M. D. Crystal chemistry of iron in two styles of metasomatism in the upper mantle. *Geochim. Cosmochim. Acta* **56**, 2579–2586 (1992).
92. Dyar, M. D., McGuire, A. V. & Ziegler, R. D. Redox equilibria and crystal chemistry of coexisting minerals from spinel lherzolite mantle xenoliths. *Am. Mineral.* **74**, 969–980 (1989).
93. Hao, X.-L. & Li, Y.-L. ^{57}Fe Mössbauer spectroscopy of mineral assemblages in mantle spinel lherzolites from Cenozoic alkali basalt, eastern China: petrological applications. *Lithos* **156–159**, 112–119 (2013).
94. Lazarov, M., Woodland, A. B. & Brey, G. P. Thermal state and redox conditions of the Kaapvaal mantle: a study of xenoliths from the Finsch mine, South Africa. *Lithos* **112**, 913–923 (2009).
95. Luth, R. W. & Canil, D. Ferric iron in mantle-derived pyroxenes and a new oxybarometer for the mantle. *Contrib. Mineral. Petrol.* **113**, 236–248 (1993).
96. McGuire, A. V., Dyar, M. D. & Nielson, J. E. Metasomatic oxidation of upper mantle periodotite. *Contrib. Mineral. Petrol.* **109**, 252–264 (1991).
97. Nimis, P., Goncharov, A., Ionov, D. A. & McCammon, C. Fe^{3+} partitioning systematics between orthopyroxene and garnet in mantle peridotite xenoliths and implications for thermobarometry of oxidized and reduced mantle rocks. *Contrib. Mineral. Petrol.* **169**, 6 (2015).
98. Woodland, A. B. Ferric iron contents of clinopyroxene from cratonic mantle and partitioning behaviour with garnet. *Lithos* **112**, 1143–1149 (2009).
99. Woodland, A. B., Kornprobst, J. & Tabit, A. Ferric iron in orogenic lherzolite massifs and controls of oxygen fugacity in the upper mantle. *Lithos* **89**, 222–241 (2006).
100. Woodland, A. B. & Peltonen, P. in *The PH Nixon volume, Proceedings of the 7th International Kimberlite Conference* 904–911 (Red Roof Design, 1999).
101. Dasgupta, R., Hirschmann, M. M. & Smith, N. D. Partial melting experiments of peridotite + CO_2 at 3 GPa and genesis of alkalic ocean island basalts. *J. Petrol.* **48**, 2093–2124 (2007).
102. Davis, F. A. & Hirschmann, M. M. The effects of K_2O on the compositions of near-solidus melts of garnet peridotite at 3 GPa and the origin of basalts from enriched mantle. *Contrib. Mineral. Petrol.* **166**, 1029–1046 (2013).
103. Davis, F. A., Humayun, M., Hirschmann, M. M. & Cooper, R. S. Experimentally determined mineral/melt partitioning of first-row transition elements (FRTE) during partial melting of peridotite at 3 GPa. *Geochim. Cosmochim. Acta* **104**, 232–260 (2013).
104. Draper, D. S. & Johnston, A. D. Anhydrous PT phase relations of an Aleutian high-MgO basalt: an investigation of the role of olivine-liquid reaction in the generation of arc high-alumina basalts. *Contrib. Mineral. Petrol.* **112**, 501–519 (1992).
105. Gaetani, G. A. & Grove, T. L. The influence of water on melting of mantle peridotite. *Contrib. Mineral. Petrol.* **131**, 323–346 (1998).
106. Grove, T. L., Holbig, E. S., Barr, J. A., Till, C. B. & Krawczynski, M. J. Melts of garnet lherzolite: experiments, models and comparison to melts of pyroxenite and carbonated lherzolite. *Contrib. Mineral. Petrol.* **166**, 887–910 (2013).
107. Kinzler, R. J. Melting of mantle peridotite at pressures approaching the spinel to garnet transition: application to mid-ocean ridge basalt petrogenesis. *J. Geophys. Res. Solid Earth* **102**, 853–874 (1997).
108. Longhi, J. Some phase equilibrium systematics of lherzolite melting: I. *Geochem. Geophys. Geosyst.* **3**, 1–33 (2002).
109. Mallmann, G. & O'Neill, H. S. C. The effect of oxygen fugacity on the partitioning of Re between crystals and silicate melt during mantle melting. *Geochim. Cosmochim. Acta* **71**, 2837–2857 (2007).
110. Mercer, C. N. & Johnston, A. D. Experimental studies of the *P–T–*H_2O near-liquidus phase relations of basaltic andesite from North Sister Volcano, High Oregon Cascades: constraints on lower-crustal mineral assemblages. *Contrib. Mineral. Petrol.* **155**, 571–592 (2008).
111. Novella, D. et al. The distribution of H_2O between silicate melt and nominally anhydrous peridotite and the onset of hydrous melting in the deep upper mantle. *Earth Planet. Sci. Lett.* **400**, 1–13 (2014).
112. Baker, M. B. & Stolper, E. M. Determining the composition of high-pressure mantle melts using diamond aggregates. *Geochim. Cosmochim. Acta* **58**, 2811–2827 (1994).
113. Bartels, K. S., Kinzler, R. J. & Grove, T. L. High pressure phase relations of primitive high-alumina basalts from Medicine Lake volcano, northern California. *Contrib. Mineral. Petrol.* **108**, 253–270 (1991).
114. Bulatov, V. K., Girnis, A. V. & Brey, G. P. Experimental melting of a modally heterogeneous mantle. *Mineral. Petrol.* **75**, 131–152 (2002).
115. Falloon, T. J., Green, D. H., O'Neill, H. S. C. & Hibberson, W. O. Experimental tests of low degree peridotite partial melt compositions: implications for the nature of anhydrous near-solidus peridotite melts at 1 GPa. *Earth Planet. Sci. Lett.* **152**, 149–162 (1997).
116. Falloon, T. J. & Danyushevsky, L. Melting of refractory mantle at 1·5, 2 and 2·5 GPa under anhydrous and H_2O-undersaturated conditions: implications for the petrogenesis of high-Ca boninites and the influence of subduction components on mantle melting. *J. Petrol.* **41**, 257–283 (2000).
117. Falloon, T. J., Danyushevsky, L. V. & Green, D. H. Peridotite melting at 1 GPa: reversal experiments on partial melt compositions produced by peridotite-basalt sandwich experiments. *J. Petrol.* **42**, 2363–2390 (2001).
118. Falloon, T. J., Green, D. H., Danyushevsky, L. V. & Faul, U. H. Peridotite melting at 1.0 and 1.5 GPa: an experimental evaluation of techniques using diamond aggregates and mineral mixes for determination of near-solidus melts. *J. Petrol.* **40**, 1343–1375 (1999).
119. Gaetani, G. A., Kent, A. J. R., Grove, T. L., Hutcheon, I. D. & Stolper, E. M. Mineral/melt partitioning of trace elements during hydrous peridotite partial melting. *Contrib. Mineral. Petrol.* **145**, 391–405 (2003).
120. Grove, T. L. et al. Fractional crystallization and mantle-melting controls on calc-alkaline differentiation trends. *Contrib. Mineral. Petrol.* **145**, 515–533 (2003).
121. Kinzler, R. J. & Grove, T. L. Primary magmas of mid-ocean ridge basalts 1. Experiments and methods. *J. Geophys. Res.* **97**, 6885 (1992).
122. Laporte, D., Toplis, M. J., Seyler, M. & Devidal, J.-L. A new experimental technique for extracting liquids from peridotite at very low degrees of melting: application to partial melting of depleted peridotite. *Contrib. Mineral. Petrol.* **146**, 463–484 (2004).
123. Laubier, M., Grove, T. L. & Langmuir, C. H. Trace element mineral/melt partitioning for basaltic and basaltic andesitic melts: an experimental and laser ICP-MS study with application to the oxidation state of mantle source regions. *Earth Planet. Sci. Lett.* **392**, 265–278 (2014).
124. Liu, X. & O'Neill, H. Partial melting of spinel lherzolite in the system CaO–MgO–Al_2O_3–SiO_2 ± K_2O at 1·1 GPa. *J. Petrol.* **45**, 1339–1368 (2004).
125. Liu, X. & O'Neill, H. The effect of Cr_2O_3 on the partial melting of spinel lherzolite in the system CaO–MgO–Al_2O_3–SiO_2–Cr_2O_3 at 1·1 GPa. *J. Petrol.* **45**, 2261–2286 (2004).
126. Pichavant, M., Mysen, B. O. & Macdonald, R. Source and H_2O content of high-MgO magmas in island arc settings: an experimental study of a primitive calc-alkaline basalt from St. Vincent, Lesser Antilles arc. *Geochim. Cosmochim. Acta* **66**, 2193–2209 (2002).
127. Pickering-Witter, J. & Johnston, A. D. The effects of variable bulk composition on the melting systematics of fertile peridotitic assemblages. *Contrib. Mineral. Petrol.* **140**, 190–211 (2000).
128. Robinson, J. A. C., Wood, B. J. & Blundy, J. D. The beginning of melting of fertile and depleted peridotite at 1.5 GPa. *Earth Planet. Sci. Lett.* **155**, 97–111 (1998).
129. Salters, V. J. M., Longhi, J. E. & Bizimis, M. Near mantle solidus trace element partitioning at pressures up to 3.4 GPa. *Geochem. Geophys. Geosyst.* **3**, 1–23 (2002).
130. Schwab, B. E. & Johnston, A. D. Melting systematics of modally variable, compositionally intermediate peridotites and the effects of mineral fertility. *J. Petrol.* **42**, 1789–1811 (2001).
131. Villiger, S. The liquid line of descent of anhydrous, mantle-derived, tholeiitic liquids by fractional and equilibrium crystallization—an experimental study at 1·0 GPa. *J. Petrol.* **45**, 2369–2388 (2004).
132. Wasylenki, L. E., Baker, M. B., Kent, A. J. R. & Stolper, E. M. Near-solidus melting of the shallow upper mantle: partial melting experiments on depleted peridotite. *J. Petrol.* **44**, 1163–1191 (2003).

Acknowledgements We thank B. Wood for donating the spinel calibration suite to the Smithsonian Institution (NMNH catalogue no. 118320), T. Rose, R. Wardell and T. Gooding for laboratory support at the Smithsonian Institution, D. Canil for fruitful discussions and comments that strengthened the manuscript, the anonymous reviewers for exceptional and constructive feedback and reviewer F. Gaillard for his thoughtful reviews and for encouraging us to develop the empirical model; his reviews led to much deeper understanding and a better manuscript. We acknowledge NSF-OCE 1433212 to E.C., NSF-OCE 1434199 and NSF-OCE 1620276 to J.M.W., an NMNH Core Grant to E.C. and NSF OCE-1560088 to E.C. that supported

Q16

Research Experiences for Undergraduates (REU) student M. Said (whom we also thank) during the pilot phase of this project. This research used samples and/or data provided by the Ocean Drilling Program (ODP).

Author contributions S.K.B.: conceptualization, methodology, software, validation, formal analysis, investigation, resources, data curation, writing—original draft, writing—review and editing, visualization, project administration. E.C.: conceptualization, methodology, resources, writing—original draft, writing—review and editing, supervision, project administration, funding acquisition. F.A.D.: methodology, validation, writing—review and editing. J.M.W.: conceptualization, resources, writing—review and editing, supervision, funding acquisition.

Competing interests The authors declare no competing interests. Q17

Additional information

Supplementary information The online version contains supplementary material available at https://doi.org/10.1038/s41586-024-07603-w.

Correspondence and requests for materials should be addressed to Suzanne K. Birner.

Peer review information *Nature* thanks Fabrice Gaillard, Laura Schaefer and the other, anonymous, reviewer(s) for their contribution to the peer review of this work. Peer reviewer reports are available.

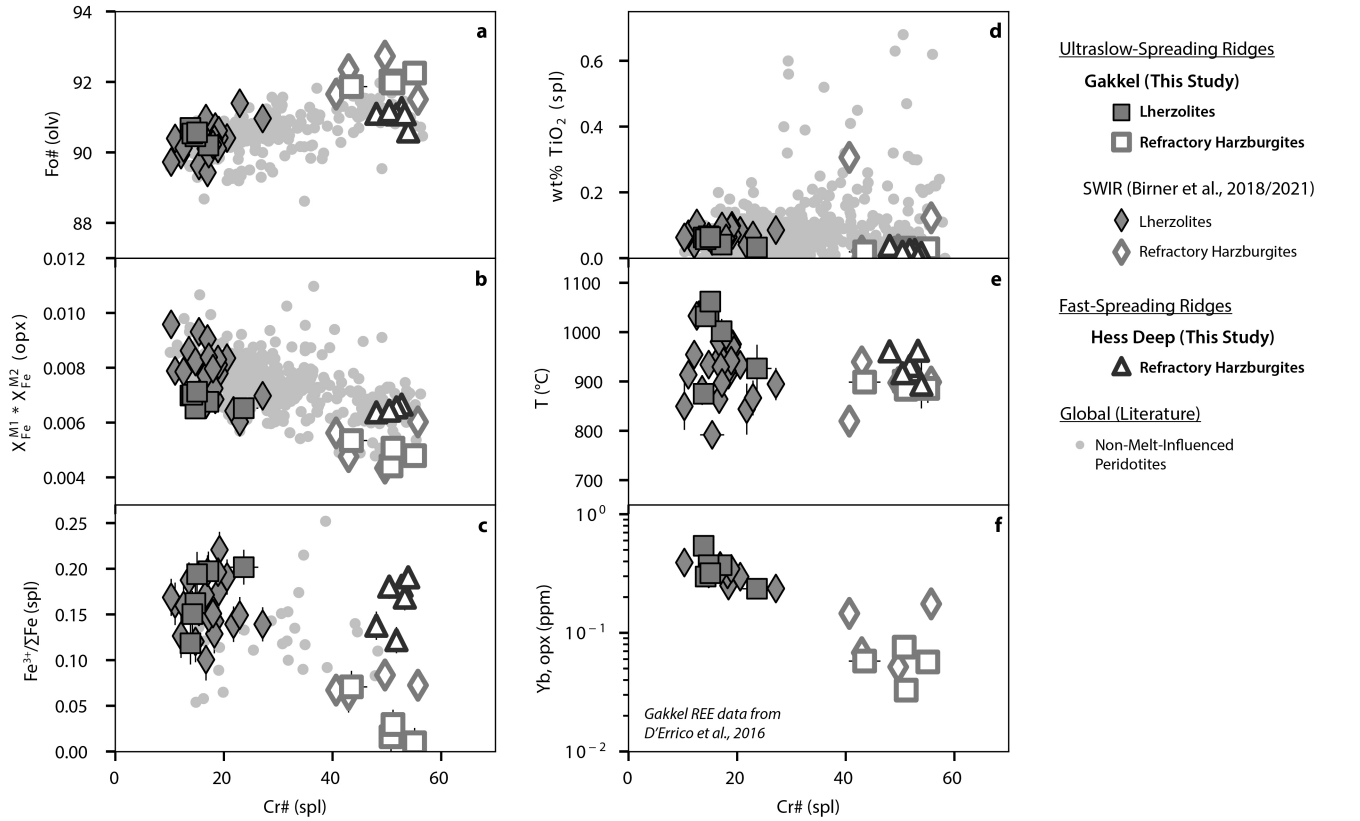

Extended Data Fig. 1 | Extended geochemistry. Geochemistry results for ridge peridotites in this study. Data for residual (non-melt-influenced) samples from the SWIR are from ref. 2, Gakkel Ridge olivine and orthopyroxene data are from ref. 32, all other data are from this study. **a**, Olivine Fo# versus spinel Cr#. Refractory harzburgites record Mg-rich compositions, consistent with their refractory nature. **b**, $X_{Fe}^{M1} X_{Fe}^{M2}$ in orthopyroxene versus spinel Cr#. Refractory harzburgites record Fe-poor compositions, consistent with their refractory nature. **c**, $Fe^{3+}/\Sigma Fe$ ratios in spinel versus spinel Cr#. The $Fe^{3+}/\Sigma Fe$ ratios in spinel are the primary driver of f_{O2} variations. Several Gakkel Ridge refractory harzburgites record values within an error of zero. **d**, TiO_2 in spinel versus spinel Cr#. The low TiO_2 content of these peridotites is one indication that they have not interacted with melts. One sample from the SWIR (KN162-9 D56-33) records slightly elevated TiO_2 but does not show the other signs of melt infiltration identified in ref. 25. **e**, Temperature versus spinel Cr#. We determined temperature using the spinel–olivine Fe–Mg exchange thermometer in ref. 68. No trends are seen between temperature and sample type. **f**, Yb in orthopyroxene versus spinel Cr#. Refractory samples record both low Yb and low Cr#, both consistent with large degrees of melt extraction. Gakkel Ridge rare earth element data are from ref. 32.

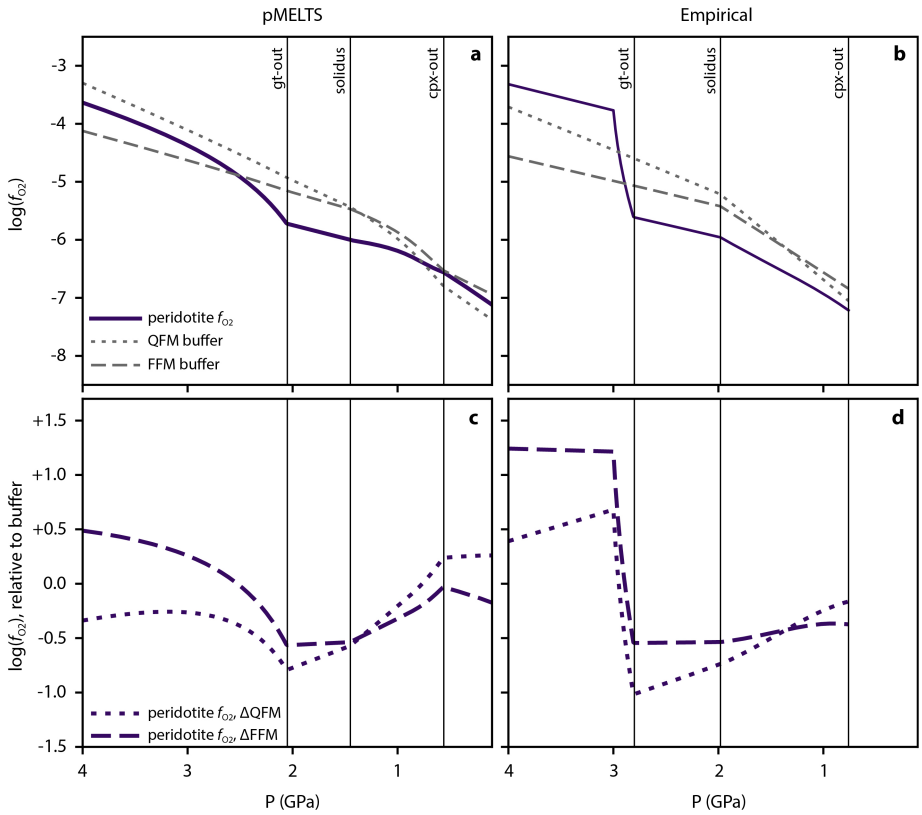

Extended Data Fig. 2 | Importance of the normalizing buffer (QFM versus FFM). The importance of the normalizing buffer when interpreting f_{O2}. **a**,**b**, Absolute log(f_{O2}) values for the QFM buffer, the FFM buffer and a peridotite residue undergoing near-fractional adiabatic decompression melting at T_p = 1,350 °C. Absolute f_{O2} was calculated for pMELTS and empirical model outputs using the empirical spinel oxybarometer of refs. 36,37. QFM was calculated at each pressure and temperature using the formulation in ref. 70; FFM was calculated using the pure-phase Gibbs free energy component of the spl–olv–opx oxybarometer as formulated in refs. 36,71 and described in ref. 37. **c**,**d**, log(f_{O2}) for the same peridotite residue, calculated relative to the QFM and FFM buffers. In the subsolidus portion of the spinel stability field, relative f_{O2} is approximately constant relative to FFM, while apparently increasing relative to QFM. In this case, ΔFFM is a more useful formulation, demonstrating that subsolidus exchange between minerals does not lead to shifts in f_{O2} in this region[51]. By contrast, the apparent increase in f_{O2} as seen when normalizing to QFM is misleading, as this change simply reflects the divergence of the QFM and FFM buffers in P–T space, as illustrated in panels **a** and **b**. Relative to QFM, f_{O2} begins to turn over around 3–4 GPa in the garnet stability field. At depths shallower than this maximum, f_{O2} is controlled primarily by the passive dilution of ferric iron in pyroxene and spinel during the garnet-to-spinel transition[51]. At depths deeper than this maximum, f_{O2} is instead primarily controlled by the stabilization of the ferric iron-bearing garnet endmember skiagite with increasing pressure[4,55].

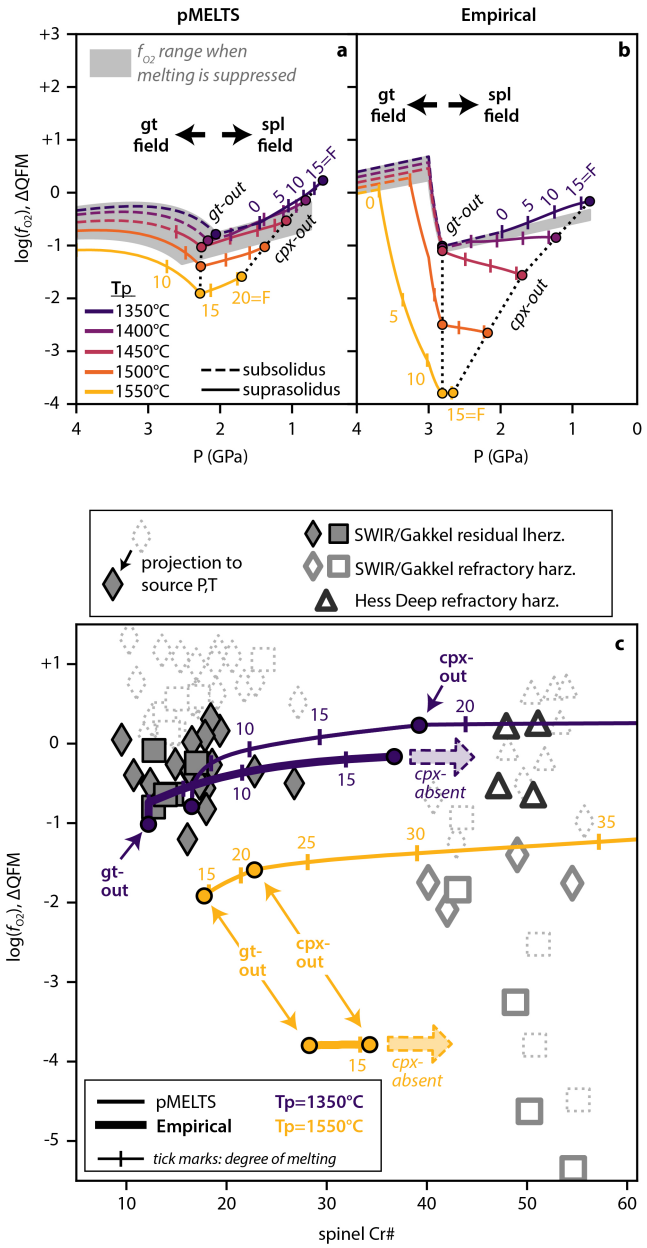

Extended Data Fig. 3 | Main-text figures plotted relative to the QFM buffer. These figures are equivalent to Figs. 2a,b and 3 but illustrate f_{O2} relative to the more commonly used QFM buffer, rather than the FFM buffer. Relative to QFM, f_{O2} seems to increase during melting in the spinel stability field. However, this increase is an artefact of the divergence in *P*–*T* space between the FFM and QFM buffers (see Extended Data Fig. 2) and does not represent a true oxidative process.

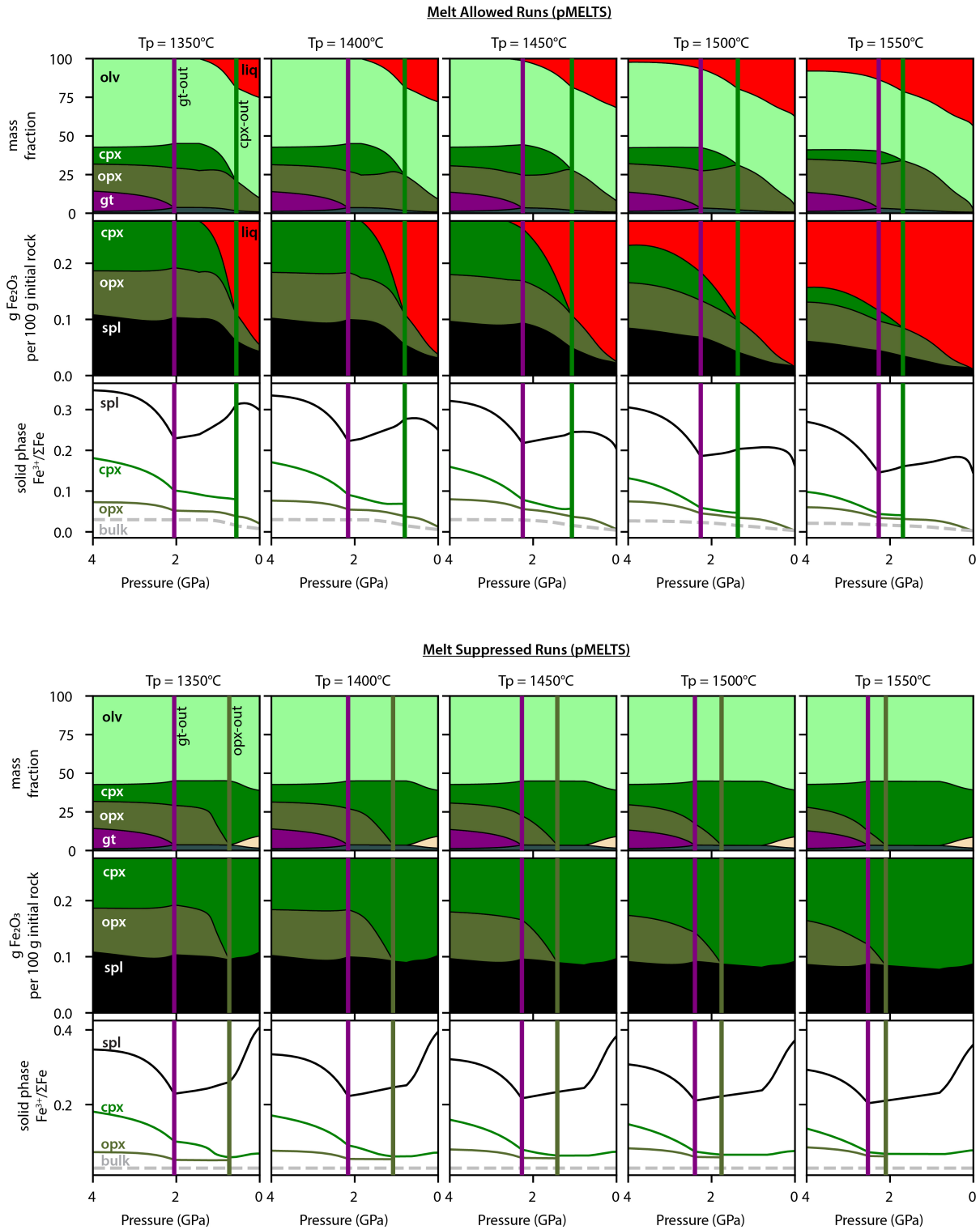

Extended Data Fig. 4 | See next page for caption.

Extended Data Fig. 4 | Graphical output of pMELTS model runs. Melt-allowed runs: Row 1: mass fraction of each phase. At higher T_p, melting initiates deeper. Both garnet-out and cpx-out shift to higher pressures at higher T_p, although garnet-out stays approximately constant once melting begins in the garnet field. Clinopyroxene mode decreases substantially at higher temperatures, in contrast to melt-suppressed runs, in which clinopyroxene mode increases. Row 2: distribution of Fe_2O_3 between phases. Most of the Fe^{3+} lost to the melt comes from the clinopyroxene phase. Row 3: ratio of ferric to total iron in bulk rock and solid phases. Whereas the bulk solid $Fe^{3+}/\Sigma Fe$ ratio decreases only slightly at higher T_p, $Fe^{3+}/\Sigma Fe$ ratios decrease substantially in spinel and pyroxene as the potential temperature increases, both in the garnet field and the spinel field. Melt-suppressed runs: Row 1: mass fraction of each phase. At higher T_p, orthopyroxene dissolves into clinopyroxene, garnet mode decreases and both garnet-out and orthopyroxene-out move to higher pressures. Plagioclase, which does not appear in melting-allowed runs, appears in melting-suppressed runs at low pressures owing to retained Al that would otherwise have been lost to the melt phase. Row 2: distribution of Fe_2O_3 between phases. At higher T_p, more Fe_2O_3 is hosted by clinopyroxene and less is hosted by orthopyroxene and spinel. Spinel exists at high pressures in pMELTS models as it is the only solid phase in the model that can incorporate Cr. The pMELTS model does not allow incorporation of Fe^{3+} into garnet, although garnet is probably a notable host of Fe^{3+} in the mantle. Row 3: ratio of ferric to total iron in each phase. Although the bulk rock $Fe^{3+}/\Sigma Fe$ ratio is constant across runs, at higher T_p, $Fe^{3+}/\Sigma Fe$ ratios decrease in spinel and clinopyroxene while staying approximately constant in orthopyroxene, reflecting transfer of Fe^{2+} from other phases, such as olivine and garnet to spinel and clinopyroxene.

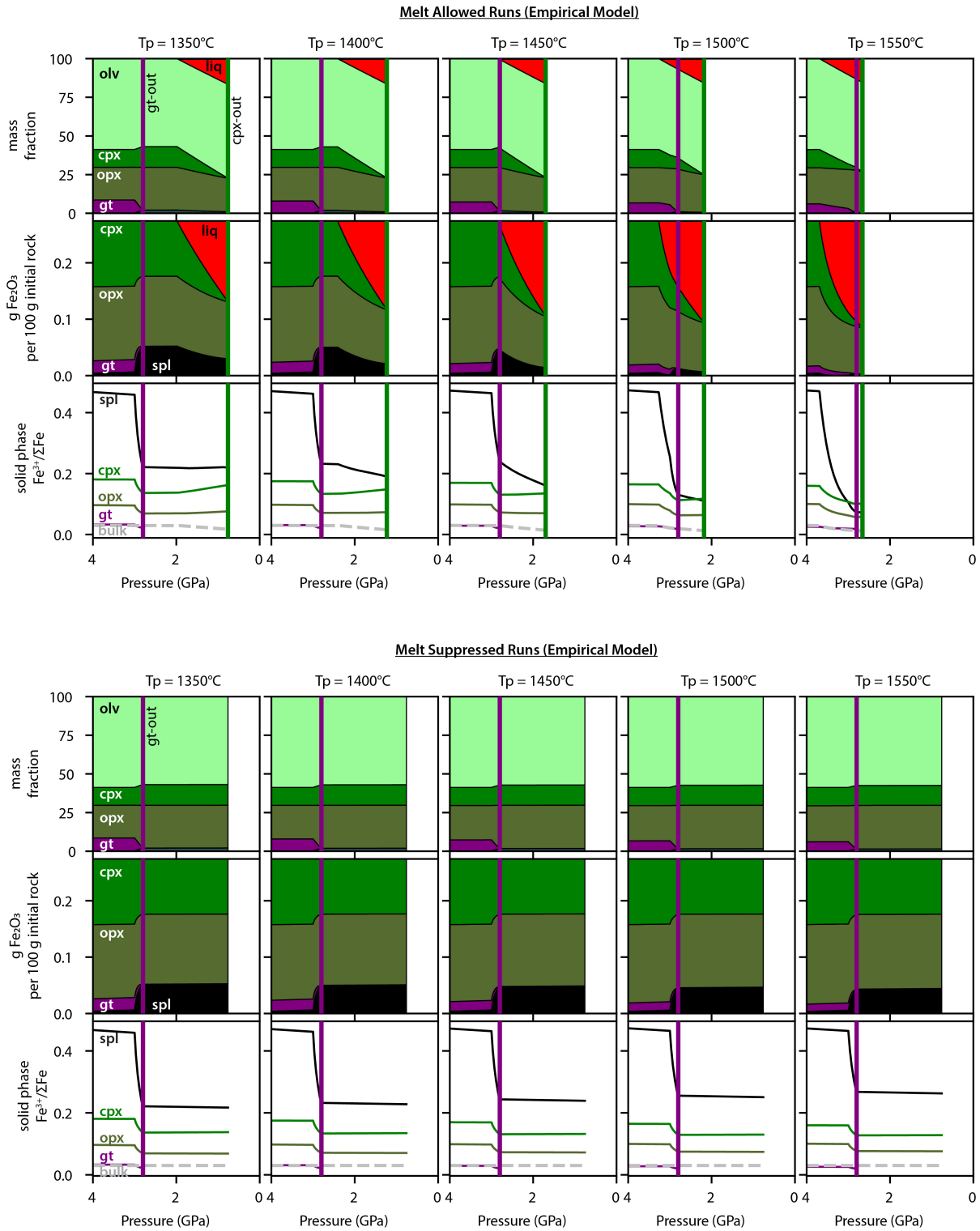

Extended Data Fig. 5 | See next page for caption.

Extended Data Fig. 5 | Graphical output of empirical model runs. Melt-allowed runs: Row 1: mass fraction of each phase. At higher T_p, melting initiates deeper and cpx-out shifts to higher pressures. Orthopyroxene mode increases slightly, whereas garnet mode decreases slightly at higher T_p, to accommodate a greater proportion of Al-bearing (Tschermak's) pyroxene components. Row 2: distribution of Fe_2O_3 between phases. Most of the Fe^{3+} lost to the melt comes from the clinopyroxene phase. Row 3: ratio of ferric to total iron between phases. Although the bulk solid $Fe^{3+}/\Sigma Fe$ ratio decreases only slightly at higher T_p, $Fe^{3+}/\Sigma Fe$ ratios decrease substantially in spinel as potential temperature increases. Melt-suppressed runs: Row 1: mass fraction of each phase. At higher T_p, garnet mode decreases. Row 2: distribution of Fe_2O_3 between phases. At higher T_p, slightly more Fe_2O_3 is hosted by orthopyroxene and slightly less is hosted by garnet. Spinel exists in small quantities (0.05 wt%) at high pressures in the empirical model to facilitate Fe^{3+} partitioning calculations (see Methods section 'Phases and components'). However, much less spinel exists in the garnet field in the empirical model than in the pMELTS model, and because the empirical model also allows ferric iron to incorporate into garnet, the amount of Fe_2O_3 hosted by spinel in the garnet field is negligible (in contrast to pMELTS, in which more than a third of the rock's Fe_2O_3 is hosted by spinel in the garnet field). Row 3: ratio of ferric to total iron in each phase. Although bulk rock $Fe^{3+}/\Sigma Fe$ is constant across all runs, at higher T_p, $Fe^{3+}/\Sigma Fe$ ratios increase slightly in spinel, while staying approximately constant in orthopyroxene and clinopyroxene, probably reflecting transfer of Fe^{2+} from other phases, such as olivine to spinel. When calculating f_{O2}, this slight increase in $Fe^{3+}/\Sigma Fe$ ratio in spinel is outweighed by the effect of temperature on magnetite activity, leading to lower f_{O2} at higher potential temperature (as shown in Fig. 2).

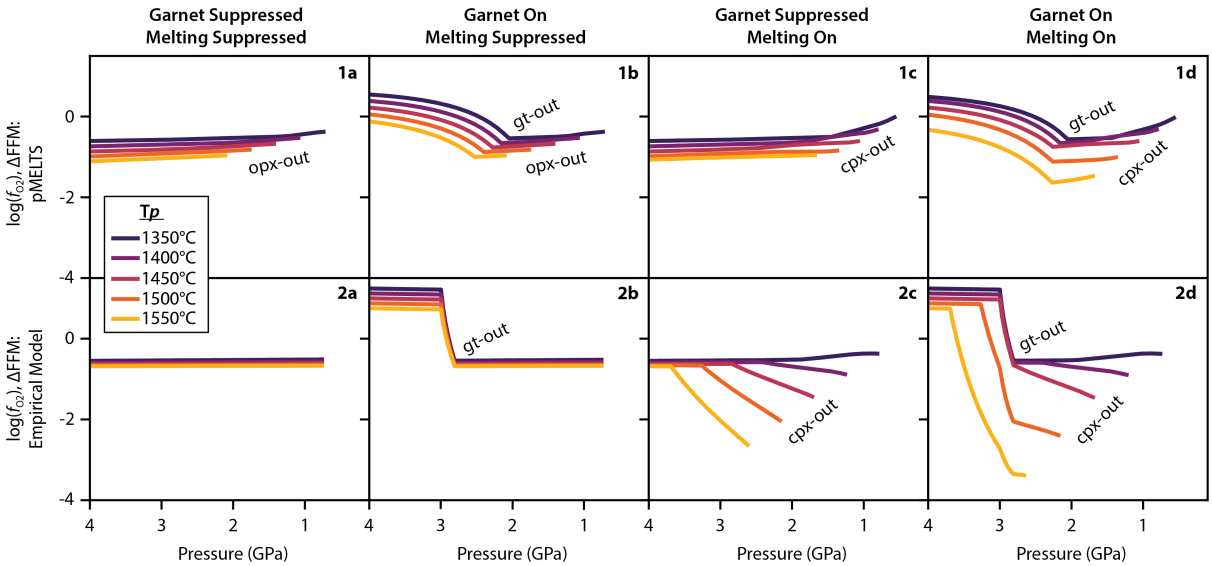

Extended Data Fig. 6 | Effects of temperature, melting and garnet. Effects of temperature, melting and garnet presence on f_{O_2} during isentropic decompression of a peridotite residue in the pMELTS model (row 1) and our empirical model (row 2). Column a, garnet-suppressed, melt-suppressed runs. In both pMELTS and our empirical model, we observe little effect on f_{O_2} as a function of either pressure or potential temperature. Subsolidus pMELTS runs truncate at opx-out, as orthopyroxene is exhausted during subsolidus reactions that dissolve orthopyroxene into clinopyroxene. Subsolidus empirical model runs end at an arbitrary pressure of 0.75 GPa. Column b, garnet-allowed, melt-suppressed runs. When garnet is allowed to form at high pressures, f_{O_2} is higher relative to the garnet-suppressed case. In both pMELTS, which puts no ferric iron in garnet, and in our empirical model, which does put ferric iron in garnet, garnet takes in less ferric iron than the equilibrium pyroxenes and spinel. Consequently, high modal garnet concentrates ferric iron in the pyroxenes and spinel and f_{O_2} increases. During decompression from the garnet field to the spinel field, f_{O_2} decreases because the concentration of ferric iron in spinel and pyroxene decreases (ferric iron is 'diluted' in these phases) as their modal proportions grow. Because bulk composition remains constant, runs end at the same f_{O_2} in the low-pressure spinel field region as they do in the garnet-suppressed, melt-suppressed case. In melt-suppressed runs, potential temperature plays a small role in varying f_{O_2}, with the effect of temperature being more pronounced in pMELTS than in the empirical model. Column c, garnet-suppressed, melt-allowed runs. Both pMELTS and the empirical model generate more reduced residues at similar degrees of melt extraction (for example, clinopyroxene-out) when melting occurs at higher T_p compared with melting at lower T_p. Column d, garnet-allowed, melt-allowed runs. These runs are equivalent to those shown in Fig. 2. In both pMELTS and the empirical model, hot melting that begins in the garnet field results in further f_{O_2} reduction relative to hot melting when garnet is suppressed. This demonstrates that high-temperature melting and garnet-field melting each play a role in developing the extremely reduced residues we observe in this study.

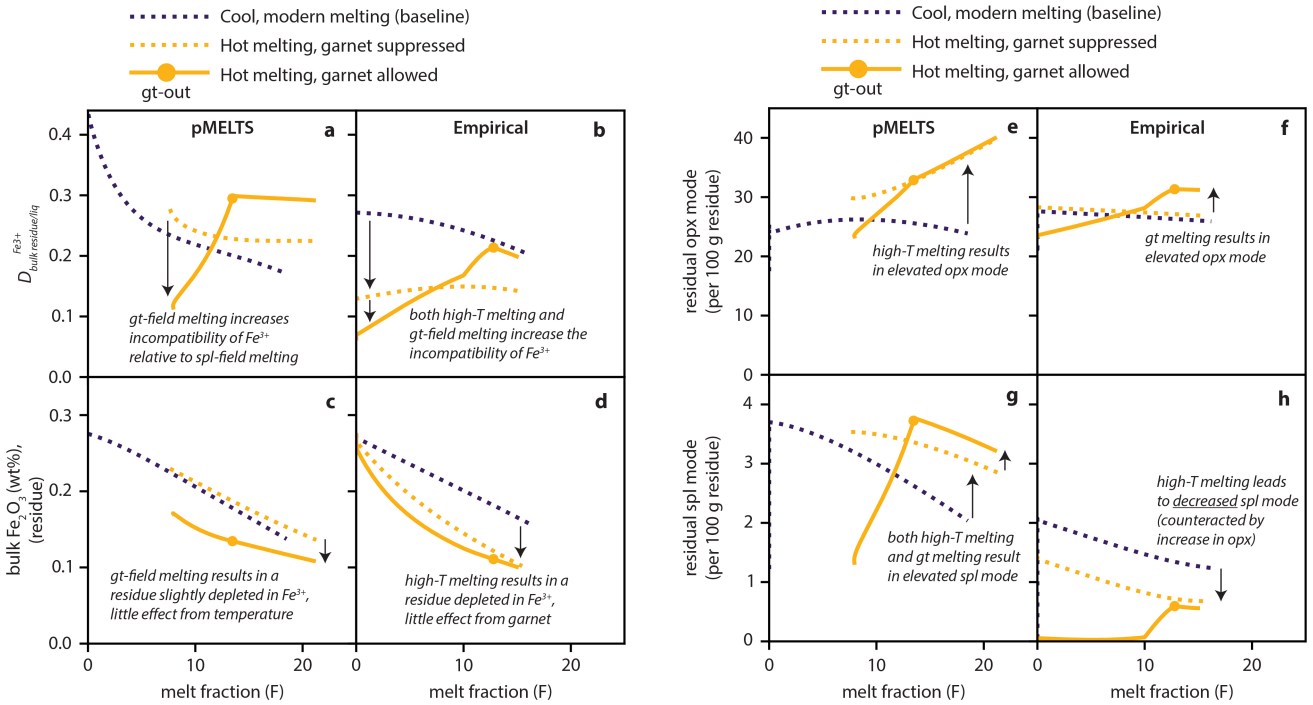

Extended Data Fig. 7 | Mechanism for reduction in residue f_{O2}. Bulk Fe_2O_3 partition coefficients (**a**,**b**), bulk Fe_2O_3 in wt% (**c**,**d**) and mineral modes (**e**–**h**) of peridotite residues output from pMELTS and our empirical model plotted against percent total melt extracted (F). Model output illustrates the mechanisms for f_{O2} reduction during melt extraction from garnet peridotite at high potential temperature. Dotted purple lines show model output for a modern ridge potential temperature (T_p = 1,350 °C) at which melting begins in the spinel field, after garnet-out. Solid orange lines show model output for a hotter potential temperature (T_p = 1,550 °C) at which melting begins in the garnet stability field. Dotted orange lines show model output for this same hot potential temperature (T_p = 1,550 °C) but with garnet stability suppressed, so the residue remains spinel peridotite at all pressures. The hot melting curves for pMELTS do not extend to F = 0 because pMELTS predicts that the peridotite is above its solidus at 4 GPa for T_p = 1,550 °C. All model output ends at clinopyroxene-out. Bulk Fe^{3+} extraction (**a**–**d**) occurs when Fe^{3+} is removed from the solid during melting owing to the incompatibility of Fe^{3+} in the bulk solid. Concentrations of Fe^{3+} in residual minerals also decrease when the relative modal abundances of pyroxenes and spinel (**e**–**h**) increase (Fe^{3+} 'dilution'). The two models are largely in agreement that both high temperatures and residual garnet are important factors in generating reduced spinel peridotite residues, although the models differ in the weights of the temperature and garnet effects.

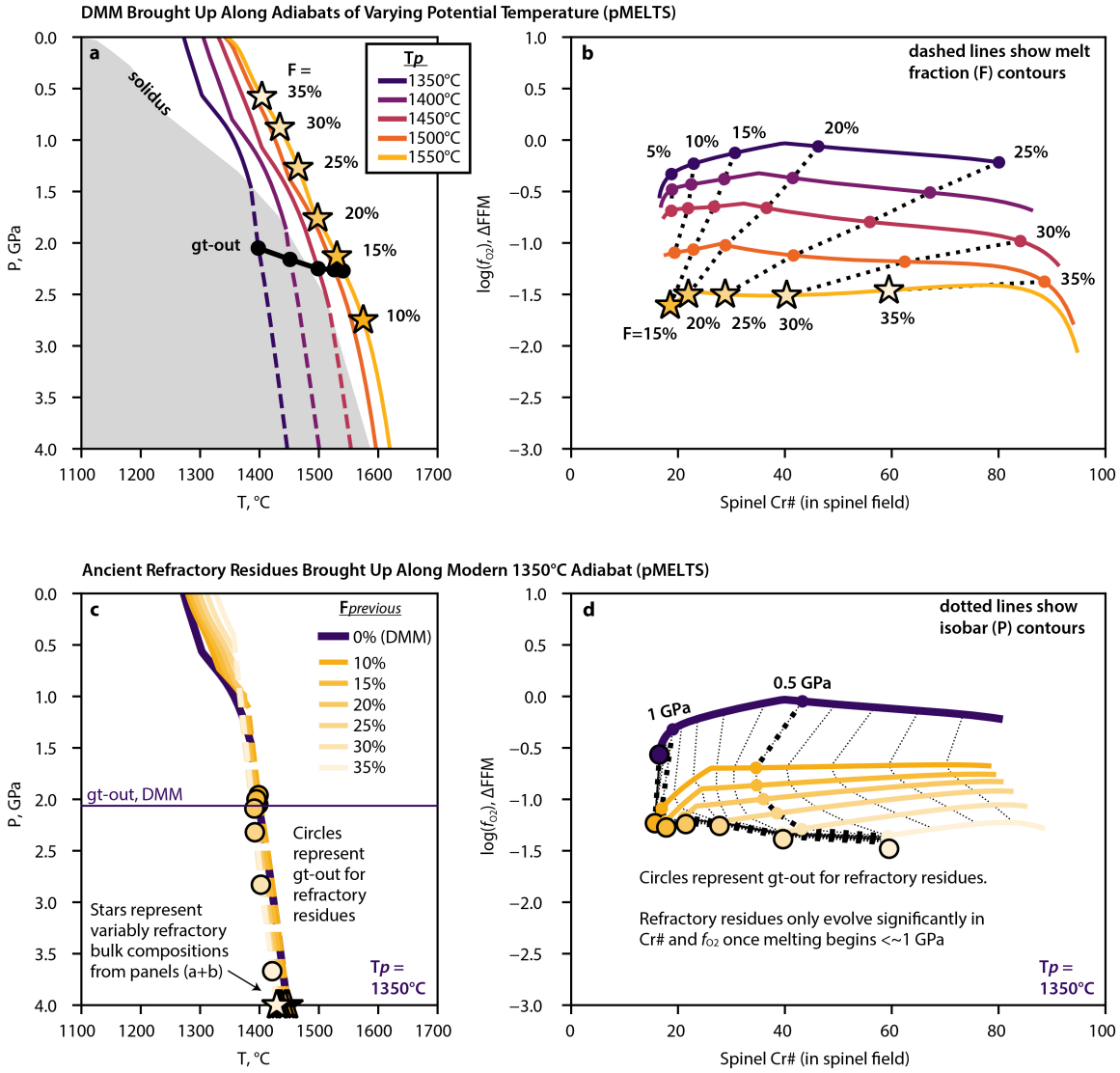

Extended Data Fig. 8 | Refractory rafts along a modern adiabat. Modelling results from pMELTS demonstrating the effect of bringing refractory residues back up along a modern geotherm. Dashed lines represent subsolidus conditions and solid lines represent conditions in which melt is present. **a**, *P*–*T* paths for pMELTS models at constant composition (DMM) and varying T_p. Subsolidus field is shown in grey and the location of garnet-out is shown as a black line. Shaded orange stars along the 1,550 °C T_p path represent locations of 10–35% melting. These bulk solid compositions are used in panels **c** and **d** to investigate the effect of previous melt depletion on f_{O2}. **b**, Oxygen fugacity of the residual solid versus spinel Cr# for the portions of the paths in panel **a** that exist in the spinel stability field. Model output at higher T_p records much lower f_{O2} than the model output at lower T_p. Spinel Cr#s consistent with low-f_{O2} peridotites at the SWIR and Gakkel Ridge (Cr# ≈ 40–60) require roughly 30–35% melting along the 1,550 °C T_p path. **c**, Bulk compositions corresponding to the shaded orange stars in panels **a** and **b**, representing varying degrees of previous melt depletion, brought up along a modern 1,350 °C adiabat. Evolution of DMM is shown for comparison (equivalent to the 1,350 °C adiabat in panel **a**). **d**, Oxygen fugacity versus spinel Cr# for varying degrees of previous depletion, brought up along a modern 1,350 °C adiabat. Evolution of DMM is shown for comparison (equivalent to the 1,350 °C adiabat in panel **b**). Peridotite residues that melted at high temperature during previous melting events retain their reduced signature when brought up beneath the modern ridge axis. Circles represent conditions at garnet-out (2–3 GPa; see panel **c**); however, the residues do not evolve substantially in Cr# and f_{O2} between garnet out and the solidus at pressures shallower than about 1 GPa. After the onset of melting, Cr# and f_{O2} begin to increase. Because these refractory residues do not begin to re-melt until such shallow conditions, they are unlikely to contribute substantially to ridge melts.

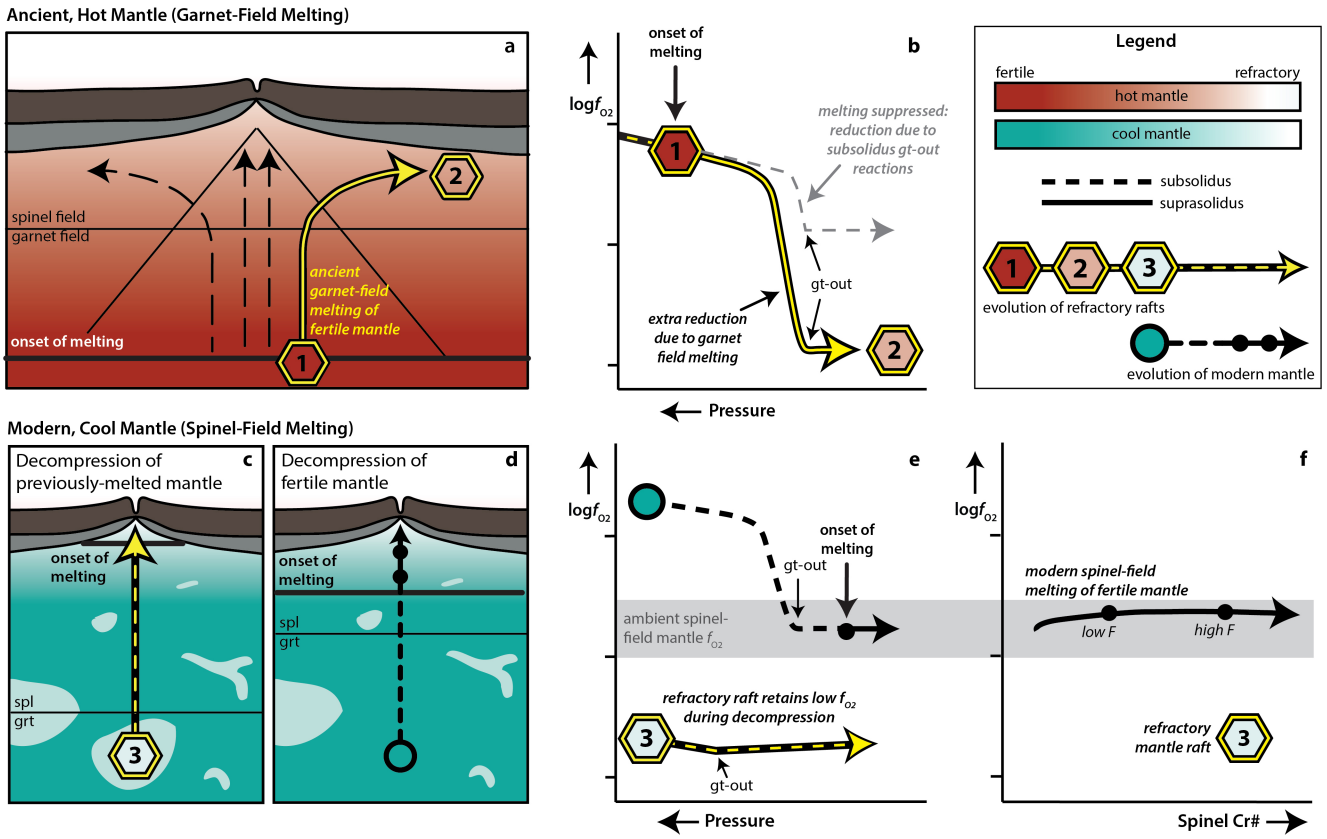

Extended Data Fig. 9 | Schematic. Schematic representation of the development of f_{O2} heterogeneities owing to ancient melting events. **a**,**b**, Ancient hot mantle, in which melting initiates in the garnet field. **a**, Ancient fertile mantle ascends along a hot adiabat, producing large degrees of melting in the garnet stability field and a refractory peridotite residue. **b**, During garnet-field melting, f_{O2} is reduced relative to an equivalent, melt-suppressed assemblage. **c**–**f**, Modern cool mantle, consisting primarily of fertile material with rafts of previously melted mantle. **c**, Rafts of refractory material produced by ancient melting (as shown in panel **a**) may re-ascend along a cool adiabat but will not experience notable further melting owing to their refractory nature. **d**, Along a cool adiabat, fertile ambient mantle material melts in the spinel stability field. The extent of melting is primarily a function of spreading rate, which determines the pressure at which melting stops. **e**,**f**, Modern, fertile mantle will not substantially change in f_{O2} during melting, although spinel Cr# will increase as melting continues[25]. Rafts of ancient, refractory material will retain their high spinel Cr# and low f_{O2} signature produced during ancient melting events.

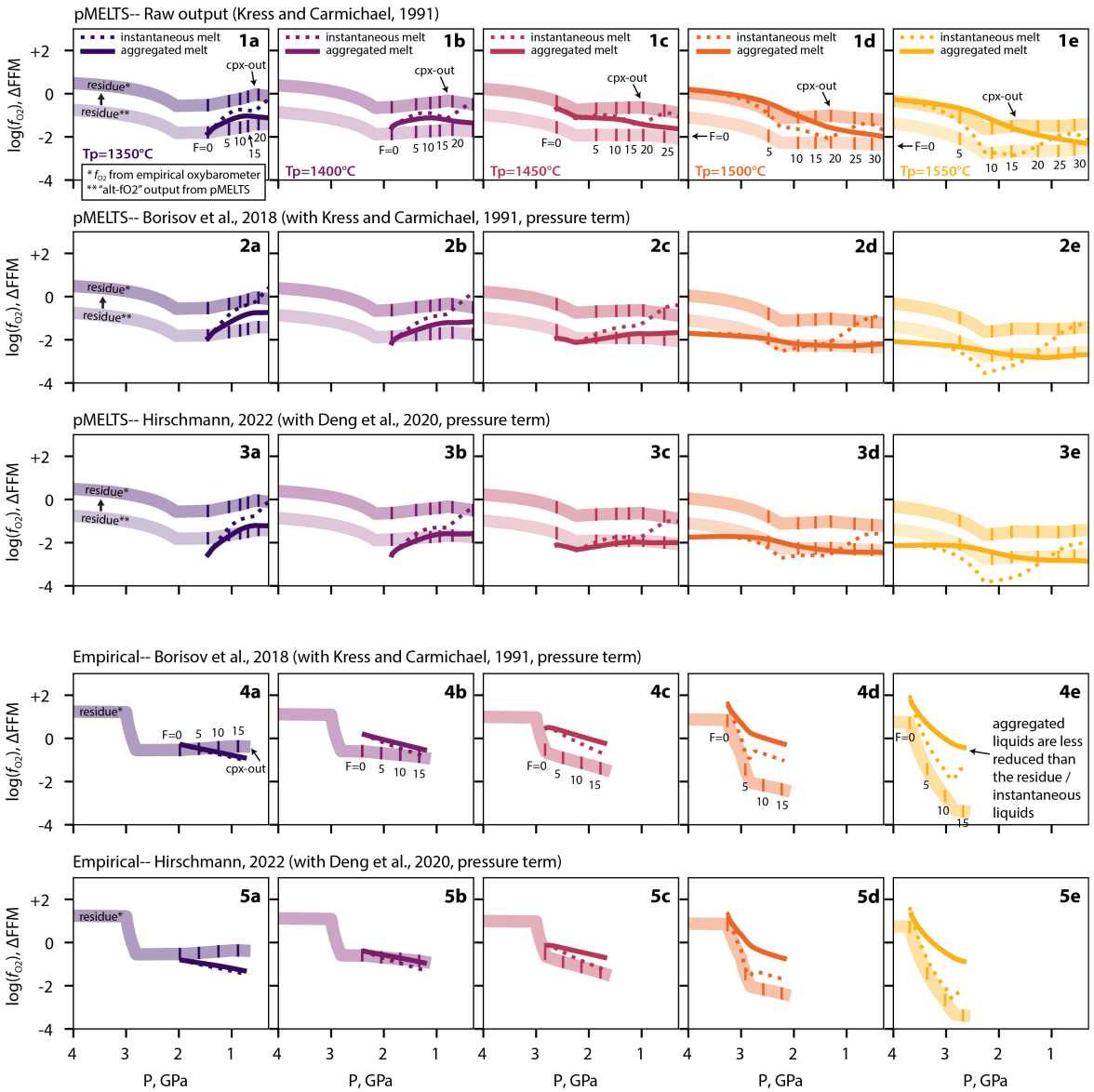

Extended Data Fig. 10 | Liquid f_{O_2}. Instantaneous/aggregated liquid f_{O_2} calculated for model runs. Differences between dotted lines (instantaneous liquids) and solid lines (aggregated liquids) demonstrate the homogenizing effect of melt aggregation. Although the residue, and thus instantaneous liquids, may reach very low f_{O_2} at high degrees of melting and high potential temperature, the aggregated liquids are less reduced owing to the influence of early, more oxidized liquids. Row 1 shows the raw pMELTS output, which calculates liquid f_{O_2} from the algorithm in ref. 79. Depending on P–T conditions, instantaneous liquids (dotted lines) may have higher or lower f_{O_2} than the f_{O_2} returned by the solid-phase assemblage using the 'alternative-fO2' tag in pMELTS (residue**) (see Methods). We also calculate f_{O_2} values from pMELTS solid-phase output using spinel oxybarometry (residue*), as applied in the main-text figures. Because ref. 79 is not well calibrated on our model compositions, we used two other methods for calculating liquid f_{O_2}: (1) the compositional framework of ref. 84 combined with the ref. 79 pressure term (rows 2 and 4) and (2) the model of ref. 87, which revises ref. 84 and applies the pressure term of ref. 88 (rows 3 and 5). These frameworks offer an improvement, although large uncertainties remain (see Methods). As well as uncertainty related to translation between melt composition and melt f_{O_2}, we emphasize that neither model forces instantaneous liquids to be in f_{O_2} equilibrium with their residues (see Methods and ref. 24 for discussion), despite that requirement in nature. Further, calculated liquid f_{O_2} values from pMELTS and our empirical model are particularly uncertain at high T_p, at which Fe^{3+}-partitioning and f_{O_2}-compositional relationships are less well constrained. Finally, liquids in our empirical model do not extend beyond cpx-out and so contributions from shallow pressures are absent. Despite these caveats and uncertainties, we expect that high-temperature, garnet-field melting could lead to aggregated liquids that are slightly more reduced than aggregated liquids from spinel-field melting, although not as reduced as the peridotite residues observed in this study owing to melt aggregation and homogenization.

Extended Data Table 1 | Phases and components (empirical model)

Phase	Formula / Stoichiometry	Oxide Components
Olivine	$(Mg^{2+},Fe^{2+})_2SiO_4$	MgO, FeO, SiO_2
Orthopyroxene	$(Ca^{2+},Mg^{2+},Fe^{2+})_{2-x}(Al^{3+},Cr^{3+},Fe^{3+})_{2x}Si_{2-x}O_6$	CaO, MgO, FeO, Al_2O_3, Cr_2O_3, Fe_2O_3, SiO_2
Clinopyroxene	$(Ca^{2+},Mg^{2+},Fe^{2+})_{2-x}(Al^{3+},Cr^{3+},Fe^{3+})_{2x}Si_{2-x}O_6$	CaO, MgO, FeO, Al_2O_3, Cr_2O_3, Fe_2O_3, SiO_2
Garnet	$(Ca^{2+},Mg^{2+},Fe^{2+})_3(Al^{3+},Cr^{3+},Fe^{3+})_2Si_3O_{12}$	CaO, MgO, FeO, Al_2O_3, Cr_2O_3, Fe_2O_3, SiO_2
Spinel	$(Mg^{2+},Fe^{2+})(Al^{3+},Cr^{3+},Fe^{3+})_2O_4$	MgO, FeO, Al_2O_3, Cr_2O_3, Fe_2O_3
Liquid	N/A	CaO, MgO, FeO, Al_2O_3, Fe_2O_3, SiO_2

Phases and components in the empirical model. The model comprises six phases and seven components. Unlike the pMELTS model, the empirical model incorporates ferric iron into the garnet phase.

Extended Data Table 2 | Constraints and degrees of freedom (empirical model)

Constraints (derived from xenolith and experimental data)

Constraint	Value	Source	Assemblages		
			All	Gt-bearing only	Liq-bearing only
Fe^{3+} constraints					
D_Fe^{3+}_gt/cpx	e^(-0.9985*ln([Al_2O_3]$_{cpx}$) + 0.6171)	Xenolith data[1]		X	
D_Fe^{3+}_opx/cpx	0.6133	Xenolith data[1]	X		
D_Fe^{3+}_spl/opx	e^(0.7321*ln([Fe_2O_3]$_{spl}$) + 1.051)	Xenolith data[1]	X		
D_Fe^{3+}_spl/liq	e^(0.87*10000/T - 4.6 + 0.24*ln([Fe_2O_3]$_{spl}$)	Ref [52]			X
Cr^{3+}, Al^{3+} constraints					
K_D_Cr^{3+}/Al^{3+}_gt/cpx	0.5595	LEPR data[2]		X	
K_D_Cr^{3+}/Al^{3+}_opx/cpx	e^((-1395/T) + 0.7933)	Ref [20]	X		
K_D_Cr^{3+}/Al^{3+}_opx/spl	e^((1/T)*(1215+3137*Cr#$_{spl}$) - 0.391)	Ref [89]	X		
Fe^{2+}, Mg^{2+} constraints					
K_D_Fe^{2+}/Mg^{2+}_olv/opx	1.1011	LEPR data[3]	X		
K_D_Fe^{2+}/Mg^{2+}_olv/cpx	1.0339	LEPR data[3]	X		
K_D_Fe^{2+}/Mg^{2+}_olv/gt	0.595	LEPR data[2]		X	
K_D_Fe^{2+}/Mg^{2+}_olv/spl	e^((-4299*Y_{Cr} - 1283)/T + 1.469*Y_{Cr} - 2.0*Y_{Fe3+} + 0.363)	Ref [68]	X		
K_D_Fe^{2+}/Mg^{2+}_olv/liq	0.3096	LEPR data[3]			X
Ca^{2+} constraints					
(CaO/MgO)_gt	0.2358*(CaO/MgO)$_{cpx}$ + 0.119	LEPR data[2]		X	
X_$(Mg,Fe)_2Si_2O_6$ in cpx	-0.2571*(10000/T) + 1.9911	LEPR data[3]	X		
Tschermak pyx constraints					
Cpx_Ts_per_6_O / Opx_Ts_per_6_O	1.2377	LEPR data[3]	X		
T°C	(cpx_Al_per_6_O + 0.41827*Cr#$_{spl}$ - 0.09266) /0.0002115	LEPR data[3]	X		
(SiO_2/Al_2O_3)_liq	-1.032*ln(cpx_Ts_per_6_O) + 1.0512	LEPR data[3]			X

Exchange Reactions (degrees of freedom)

Exchange Reaction	Assemblages		
	All	Gt-bearing only	Liq-bearing only
3+ cation exchange (Cr^{3+}, Al^{3+}, Fe^{3+})			
Fe^{3+}-Al^{3+}, opx-cpx	X		
Cr^{3+}-Al^{3+}, opx-cpx	X		
Fe^{3+}-Al^{3+}, spl-opx	X		
Cr^{3+}-Al^{3+}, spl-opx	X		
Fe^{3+}-Al^{3+}, gt-opx		X	
Cr^{3+}-Al^{3+}, gt-cpx		X	
Fe^{3+}-Al^{3+}, liq-opx			X
2+ cation exchange (Mg^{2+}, Fe^{2+}, Ca^{2+})			
Fe^{2+}-Mg^{2+}, olv-opx	X		
Fe^{2+}-Mg^{2+}, olv-cpx	X		
Ca^{2+}-Mg^{2+}, cpx-opx	X		
Fe^{2+}-Mg^{2+}, spl-opx	X		
Fe^{2+}-Mg^{2+}, gt-opx		X	
Ca^{2+}-Mg^{2+}, gt-cpx		X	
Fe^{2+}-Mg^{2+}, liq-opx			X
Tschermak exchange (X^{2+} + Si^{4+} <-> $Al^{3+}Al^{3+}$)			
$Al^{3+}Al^{3+}$-$Mg^{2+}Si^{4+}$, opx-cpx	X		
spl+opx <-> olv+Ts-opx	X		
$Al^{3+}Al^{3+}$-$Mg^{2+}Si^{4+}$, opx-liq			X

T in K for all equations

[1]Ferric-bearing xenolith citations: Refs 90–100
[2,3]LEPR data refers to experimental data compiled from the Library of Experimental Phase Relations [Ref 101]. Below we list citations for all studies included in our compilations:
[2]LEPR citations for experiments containing [gt+olv+opx+cpx+liq]: Refs 102–113
[3]LEPR citations for experiments containing [spl+olv+opx+liq]: Refs 52,104-108,114–135

Constraints and degrees of freedom for the empirical model. Constraints take the form of partitioning relationships and are derived from natural peridotite xenolith datasets and experimental datasets. Exchange reactions allow each phase to vary, so as to fulfil the compositional constraints at each model step[82,89–132].

Extended Data Table 3 | Garnet-out reactions (empirical model)

Simplified Reaction	Balanced Reaction (written in terms of Mg, Al endmembers for simplicity)	Reaction weight
Gt + Olv → Spl + 2*Opx	$Mg_3Al_2Si_3O_{12} + Mg_2SiO_4 \rightarrow MgAl_2O_4 + 2*Mg_2Si_2O_6$	x[1]
Gt → Opx + Ts-Opx	$Mg_3Al_2Si_3O_{12} \rightarrow Mg_2Si_2O_6 + MgAl_2SiO_6$	2x
Ca-Gt + Olv → Spl + 2*Cpx	$Ca_2MgAl_2Si_3O_{12} + Mg_2SiO_4 \rightarrow MgAl_2O_4 + 2*CaMgSi_2O_6$	x*Ca_ratio[2]
Ca-Gt → Cpx + Ts-Cpx	$Ca_2MgAl_2Si_3O_{12} \rightarrow CaMgSi_2O_6 + CaAl_2SiO_6$	2x*Ca_ratio[2]

[1]where x represents an arbitrary amount of garnet consumed by the reaction

[2]where Ca_ratio is the ratio of Ca-gt to (Fe,Mg)-garnet endmembers within the garnet phase

Garnet-out reactions used in the empirical model. Reactions consume garnet (±olivine) produce either orthopyroxene or clinopyroxene (±spinel).